The Journal of Physiology

Human-derived cardiac-neural microtissues reveal catecholaminergic polymorphic ventricular tachycardia is also a disease of the sympathetic neuron

Ni Li[1,2], Chenchen Zhang[3], Mengying Xu[3], YoonYoung Choi[1], Davi Sidarta-Oliveira[1], Ruirui Dong[3], Xinyu Hu[3], Enrique M. Toledo[4], Cesar A. Prada-Medina[4], Finbar Argus[5], Kun Liu[1], Mingyu Li[6], Linna Zhou[6,7], Hagan Bayley[6], Corey Smith[8], Chris Denning[9], Ana I. Domingos[1], Guoliang Hao[1,3], Dan Li[1] and David J. Paterson[1]

[1]*Burdon Sanderson Cardiac Science Centre and BHF Centre of Research Excellence, Department of Physiology, Anatomy and Genetics, University of Oxford, Oxford, UK*
[2]*Sun Yat-Sen Memorial Hospital, Sun Yat-Sen University, Guangzhou, China*
[3]*Institute of Electrophysiology, Henan Academy of Innovations in Medical Science, Zhengzhou, China*
[4]*Novo Nordisk Research Centre Oxford, Innovation Building, Oxford, UK*
[5]*Auckland Bioengineering Institute, University of Auckland, Auckland, New Zealand*
[6]*Department of Chemistry, University of Oxford, Oxford, UK*
[7]*Ludwig Institute for Cancer Research, Nuffield Department of Medicine, University of Oxford, Oxford, UK*
[8]*School of Medicine, Case Western Reserve University, Cleveland, OH, USA*
[9]*University of Nottingham Biodiscovery Institute University Park, Nottingham, UK*

Handling Editors: Natalia Trayanova & Crystal Ripplinger

The peer review history is available in the Supporting information section of this article (https://doi.org/10.1113/JP290024#support-information-section).

Ni Li holds an MD degree from Peking Union Medical College, and a DPhil degree in Physiology, Anatomy, and Genetics from the University of Oxford. Her research is focused on using hiPSC-derived cardiac myocytes and sympathetic neurons for disease modelling, specifically exploring the pathological mechanisms of catecholaminergic polymorphic ventricular tachycardia (CPVT) and the pathogenic role of CPVT neurons in cardiac disorders.

D. Li and D. J. Paterson are joint senior authors

 DOI: 10.1113/JP290024

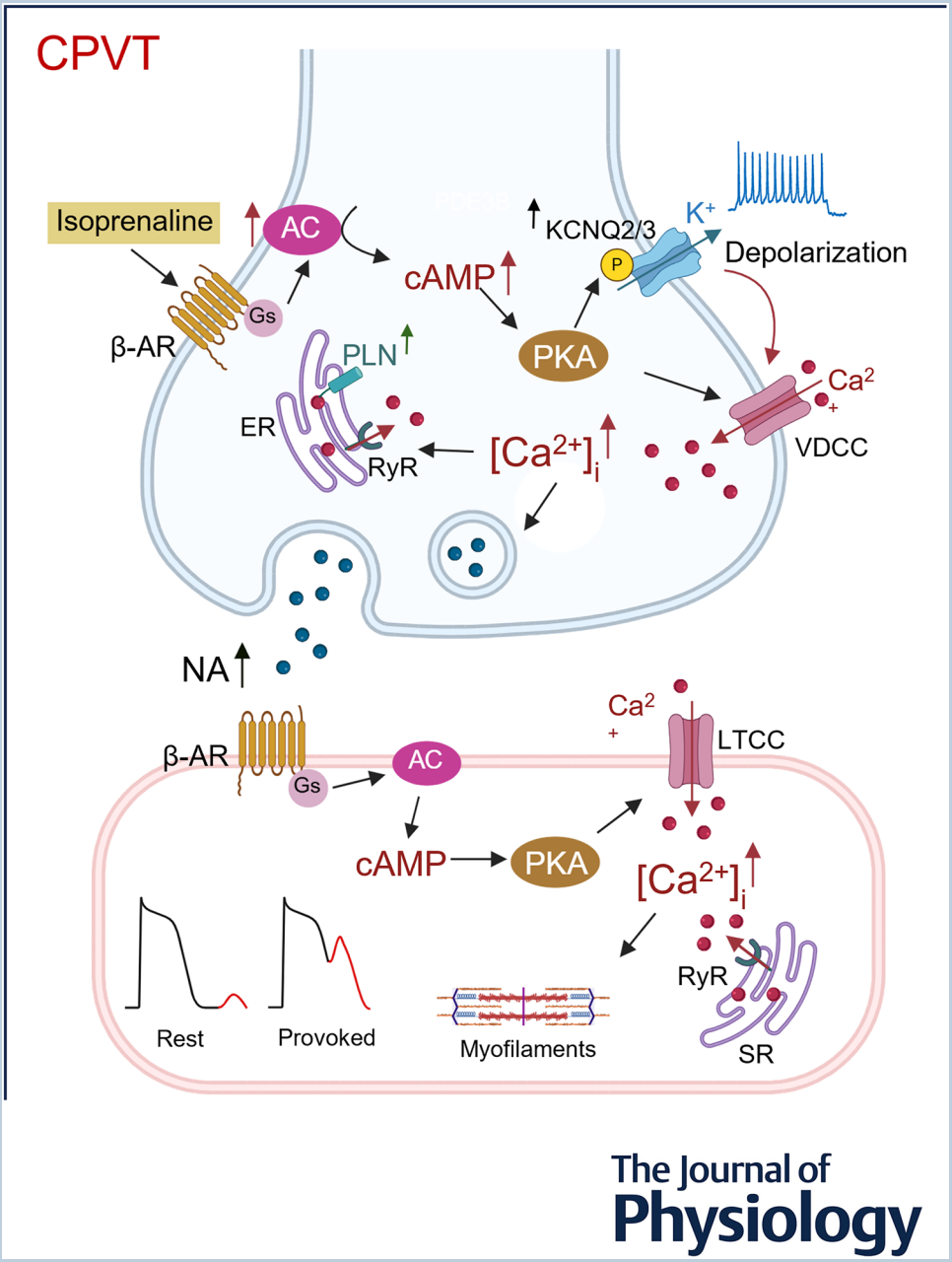

Abstract figure legend Schematic diagram illustrating the proposed pathway in which regulatory defects might occur in sympathetic neurons derived from hiPSC in catecholaminergic polymorphic ventricular tachycardia (CPVT). Specifically, enhanced calcium transients appeared to derive from three sources: enhanced membrane excitability (due to loss of function mutation of *KCNQ2/3* and its downregulation), increased β-receptor-activated adenylyl cyclase elevating cAMP, and increased phospholamban (PLN) leading to greater inhibition of endoplasmic reticulum calcium ATPase and shortened calcium re-uptake. This may predispose to higher levels of transmission as indicated by the increased cAMP response that directly triggers arrhythmias in healthy cardiomyocytes. Therefore, CPVT should be redefined as a neuro-cardiac disorder.

Abstract Sudden cardiac death in young individuals with structurally normal hearts represents a critical unresolved clinical challenge and typically occurs in patients with inherited arrhythmia syndromes due to cardiac channelopathies. Catecholaminergic polymorphic ventricular tachycardia

(CPVT) can cause fatal arrhythmias triggered by adrenergic stimulation. Therapeutic interventions primarily target cardiac myocytes (CMs) despite robust clinical evidence demonstrating the life-saving efficacy of cardiac sympathetic denervation. To understand this therapeutic paradox, we developed human induced pluripotent stem cell (hiPSC)-derived CMs and sympathetic neurons (SNs) from healthy individuals and CPVT patients to investigate neurocardiac interactions using two- and three-dimensional microtissue models. We tested the hypothesis that CPVT is also a disease of the autonomic nervous system and observed that CPVT hiPSC-derived SNs had enhanced calcium transients, elevated cyclic adenosine monophosphate levels, and hyperexcitability, similar to diseased cardiomyocytes. Critically, co-culturing diseased neurons with healthy CMs induced arrhythmogenic activity, establishing that neuronal dysfunction directly triggers cardiac arrhythmias. Multielectrode array recordings, optical mapping and single-cell RNA sequencing revealed dysregulated neurotransmitter pathways and identified druggable molecular targets within SNs. These findings may explain why surgically interrupting sympathetic nerves helps CPVT patients and identify the nervous system as a therapeutic target. They further suggest that CPVT is more than a disease of the CM and should be re-defined as a neuro-cardiac disorder that paves the way for neuromodulation therapy.

(Received 28 August 2025; accepted after revision 16 January 2026; first published online 16 February 2026)
Correspondence authors D. Li and D. J. Paterson: Burdon Sanderson Cardiac Science Centre and BHF Centre of Research Excellence, Department of Physiology, Anatomy and Genetics, University of Oxford, Oxford, OX1 3PT, UK. Email: dan.li@dpag.ox.ac.uk and david.paterson@dpag.ox.ac.uk

Key points

- Sympathetic nerve overactivity is pro-arrhythmic and a key contributor to ventricular tachycardia and sudden cardiac death in patients with cardiac channelopathies.
- Catecholaminergic polymorphic ventricular tachycardia (CPVT) sympathetic neurons (SNs) exhibit enhanced calcium transients, elevated cAMP levels, and hyperexcitability that directly trigger arrhythmias in healthy cardiomyocytes.
- Novel human induced pluripotent stem cell-derived cardiac-neural microtissue models reveal CPVT is also a neurological disorder involving dysfunctional neurocardiac interactions.
- Single-cell RNA sequencing identifies dysregulated neurotransmitter pathways in SNs, providing new therapeutic targets for neuromodulation therapy.

Introduction

Genetic mutations affecting ion channels in myocardial cell membranes, crucial for cardiac action potential generation and propagation, can predispose individuals to life-threatening arrhythmias (e.g. Schwartz et al., 2020; Webster & Berul, 2013). These channelopathies are predominately linked to different genetic disorders involving loss-of-function mutations leading to abnormal repolarisation (long QT syndrome; Modell & Lehmann, 2006), or gain of function mutations in the sarcoplasmic reticulum resulting in impaired intracellular calcium homeostasis (catecholaminergic polymorphic ventricular tachycardia; CPVT; Coumel et al., 1978; Park et al., 2019; Pérez-Riera et al., 2018; Roston, Haji-Ghassemi et al., 2018; Wleklinski et al., 2020). Common to both channelopathies is the observation that physiological stress can often provoke sudden, lethal arrhythmias in structurally normal hearts (Hayashi et al., 2009; Priori et al., 2001). CPVT is particularly significant as a cause of sudden cardiac death (SCD) in the young, despite its relatively low prevalence (1 in 5000–10,000) (Aggarwal et al., 2024; Wleklinski et al., 2020). Left untreated, mortality can reach 30–50% by the age of 40 years (Aggarwal et al., 2024), with current clinical pharmacological management still leaving approximately 10–30% of patients at risk of severe, potentially life-threatening arrhythmic events (Mazzanti et al., 2022).

CPVT arises from mutations affecting the calcium release unit in the sarcoplasmic membrane, particularly ryanodine receptor 2 (RyR2 – CPVT1) (Paudel et al., 2024) and associated proteins (triadin, junctin,

calmodulin, calsequestrin – CPVT2) (Wleklinski et al., 2020) that regulate intracellular calcium dynamics in cardiac muscle cells (Liu et al., 2008; Roston, Haji-Ghassemi et al., 2018; Wleklinski et al., 2020). Consequentially, many therapies are aimed at targeting RyR receptors. In particular flecainide (Kryshtal et al., 2021) and the stabilising protein calstabin2 (Wehrens et al., 2004) have been successful in pre-clinical models with some success in the clinic. Enhanced sympathetic activity, seen during exercise (Hayashi et al., 2009) or emotional stress (Kim et al., 2020), can trigger arrhythmias in CPVT patients by phosphorylating RyR2 receptors (Park et al., 2019), which increases calcium release (Park et al., 2019) and thus facilitates delayed afterdepolarisations (Marks et al., 2002). Beta-adrenergic blockade is therefore the current first line treatment for CPVT patients (Aggarwal et al., 2024; Kim et al., 2020), with resistant cases progressing to more radical treatments involving cardiac stellectomy (de Ferrari et al., 2015) and implantable defibrillators (ICDs) (Roston, Jones et al., 2018). However, these interventions are not without significant off-target side effects (Mazzanti et al., 2022; Roston, Jones et al., 2018).

Emerging thinking suggests that more refined site-specific targeting of the cardiac sympathetic nervous system might provide improved therapeutic utility (e.g. Habecker et al., 2025; Herring et al., 2019; Paton et al., 2025), since elevated sympathetic drive is a potent negative prognostic indicator for morbidity and mortality associated with arrhythmias and SCD in these patients (Herring et al., 2019; Larsen et al., 2016). Interestingly, sympathetic dysautonomia is a common feature of several primary cardiovascular diseases. This results in abnormal neurotransmission profiles in many species (Khemani & Mehdirad, 2020; Lu et al., 2015), which is linked to impaired cyclic nucleotide signalling (Li, Liu et al., 2022; Mishra et al., 2025) and increased membrane excitability (Davis et al., 2020) leading to abnormal intracellular calcium transients (Joca et al., 2020; Li et al., 2012) and exocytosis (Grassi & Drager, 2024). Indeed, is CPVT also a disease of the sympathetic nervous system that results in enhanced neuronal hyperexcitability? Although extensive studies have examined cardiac myocytes (CMs) derived from human induced pluripotent stem cells (hiPSCs) with CPVT genetic defects (Begovic et al., 2024; Gao et al., 2023; Itzhaki et al., 2012), little attention has been paid to understanding the role of coupled neurons as key drivers of the cardiac phenotype and whether they present an opportunity for therapeutic targeting.

Here, we derived CMs (hiPSC-CMs) and sympathetic neurons (hiPSC-SNs) from patients with a CPVT genotype to establish two- (2D) and three- (3D) dimensional co-culture models, enabling the study of neurocardiac interactions in triggered arrhythmia. We hypothesised that a diseased phenotype also resides in CPVT neurons as well as CMs, and this dysregulation may occur at several sites involving loss of intracellular calcium homeostasis. Furthermore, we performed single-cell RNA sequencing (scRNAseq) on hiPSC-CMs and hiPSC-SNs differentiated from four hiPSC lines, healthy control and CRISPR-corrected CPVT versus mutation-introduced CPVT and patient-derived CPVT. Here, we examined the transcriptomic profiles to identify key transcripts associated with dysautonomia, as a foundation for neuromodulation therapy target discovery. Some of these results have been published as abstracts (Li, Li et al., 2022, 2023).

Methods

Ethical approval

The two hiPSC isogenic pairs ($CP1^{RYR2\text{-}6737\text{-}T/C}$, $CP1^{RYR2\text{-}Corr}$, $ReBl\text{-}PAT^{RYR2\text{-}13489C/T}$ and $ReBl\text{-}PAT^{RYR2\text{-}WT}$) were provided by University of Nottingham Biodiscovery Institute. The isolation and use of patient fibroblasts were approved by the Nottingham Research Ethics Committee (License 09/H0408/74), and sample collections were registered with the UK Clinical Research Network under project 8164. The healthy iPS-OX1-19 line from the Oxford Parkinson's Disease Centre has ethics approval for control donors obtained from the National Health Service, Health Research Authority, NRES Committee South Central, Berkshire, UK (REC 10/H0505/71). Gibco episomal hiPSC line from Thermo Fisher Scientific had ethical licence/patient consent: −45 CFR Part 46, 42 CFR Part 482. The CPVT line UKKi007-A was derived from dermal fibroblasts of a CPVT-afflicted patient carrying a *de novo* heterozygous autosomal dominant p.F2483I mutation in RYR2 (Fatima et al., 2011), provided by the European Collection of Authenticated Cell Cultures and ethically approved by the Ethics Committee of the Ruhr-University Bochum, Bad Oeynhausen, Germany (Registration No. 41/2008).

hiPS cell differentiation

hiPSC cell lines. Four control hiPSC lines ($CP1^{RYR2\text{-}Corr}$, $ReBl\text{-}PAT^{RYR2\text{-}WT}$, iPS-OX1-19 and Gibco episomal hiPSC line (A18945)) and three CPVT hiPSC lines ($CP1^{RYR2\text{-}6737\text{-}T/C}$, $ReBl\text{-}PAT^{RYR2\text{-}13489C/T}$ and UKKi007-A) were employed for the differentiation of both CMs and SNs in this study. Specifically, $CP1^{RYR2\text{-}Corr}$ and $CP1^{RYR2\text{-}6737\text{-}T/C}$ were used for scRNA seq, immunofluorescence staining and calcium imaging experiments; $ReBl\text{-}PAT^{RYR2\text{-}WT}$ and $ReBl\text{-}PAT^{RYR2\text{-}13489C/T}$ were used for scRNA seq; and the iPS-OX1-19 line, Gibco A18945 and CPVT line UKKi007-A were used for calcium imaging, FRET, MEA, optical mapping and patch clamp experiments (Fig. 1). $CP1^{RYR2\text{-}6737\text{-}T/C}$, derived

from CPVT patient fibroblasts, carries a heterozygous S2246L mutation in the *RYR2* gene, while CP1$^{RYR2\text{-}Corr}$ is a derivative of the diseased genotype with edited correction of the point mutation (6737 T/C to 6737 C). ReBl-PAT$^{RYR2\text{-}WT}$ is a control cell line reprogrammed from healthy donor fibroblasts, while ReBl-PAT$^{RYR2\text{-}13489C/T}$ is a derivative with an edited mutation on base 13,489 (C/T), resulting in a 4497 arginine to cysteine mutation.

Cardiac myocyte differentiation. After thawing, iPSCs underwent three passages before being seeded onto Matrigel-coated 12-well plates, where they were cultured in mTeSR medium until reaching 85–90% confluence. The differentiation process began on Day 0, with a medium switch to RPMI/B27-insulin (Thermo Fisher Scientific, Altrincham, Cheshire, UK) (RB−) supplemented with 6 μM CHIR99021 (TOCRIS) for a 48-h incubation period. Subsequently, the medium was changed to RB− on Day 2. On Day 3, 2.5 μM Wnt-C59 (Tocris, Abbindon, UK) was introduced in RB− for another 48 h. Starting from Day 5, cells were nourished with RB− and the medium was refreshed every 2 days. The purification phase involved changing the medium to RPMI-glucose/B27 (Thermo Fisher Scientific) supplemented with 5 mM sodium L-lactate (Sigma-Aldrich, Darmstadt, Germany) from Days 11 to 14. Following purification, hiPSC-CMs were maintained in RPMI/B27 medium (RB+) from Day 15 onwards.

Sympathetic neuron differentiation. After three passages, hiPSCs were seeded on a Matrigel-coated 12-well plate and cultured in mTeSR until 80% confluent. Then a series of chemical compounds were added sequentially [500 nM LDN193189 (Sigma) Days 0–3, 10 μM SB431542 (Sigma) Days 0–4, 3 μM CHIR99021 + 10 μM DAPT (GSI-IX) (Sigma) + 0.2 μM PD173074 (Sigma) Days 2–7, 60 ng/ml Shh C25II (Thermo Fisher Scientific) + 1 μM PMP (Purmophamine) (Sigma) Days 3–12, 10 ng/ml BMP4 (Bone Morphogenic Protein 4) (R&D Systems, Minneapolis, MN, USA) Days 10–14] to culture medium to modified Pathways including Wnt signaling, TGF-β pathway, Hedgehog signaling, AKT signaling, Notch signaling, and BMP signaling. Culture medium mTeSR was gradually replaced by N2 medium [Neurobasal plus medium (Thermo Fisher Scientific) supplemented with 2 mM L-glutamine, B-27 Plus (Thermo Fisher Scientific), N2 supplements (Thermo Fisher Scientific), 0.2 mM ascorbic acid (Sigma), 0.2 nM dbcAMP (Sigma), 10 ng/ml NGF (Bio-Techne, Abbindon, UK), 10 ng/ml brain-derived neurotrophic factor (BDNF)

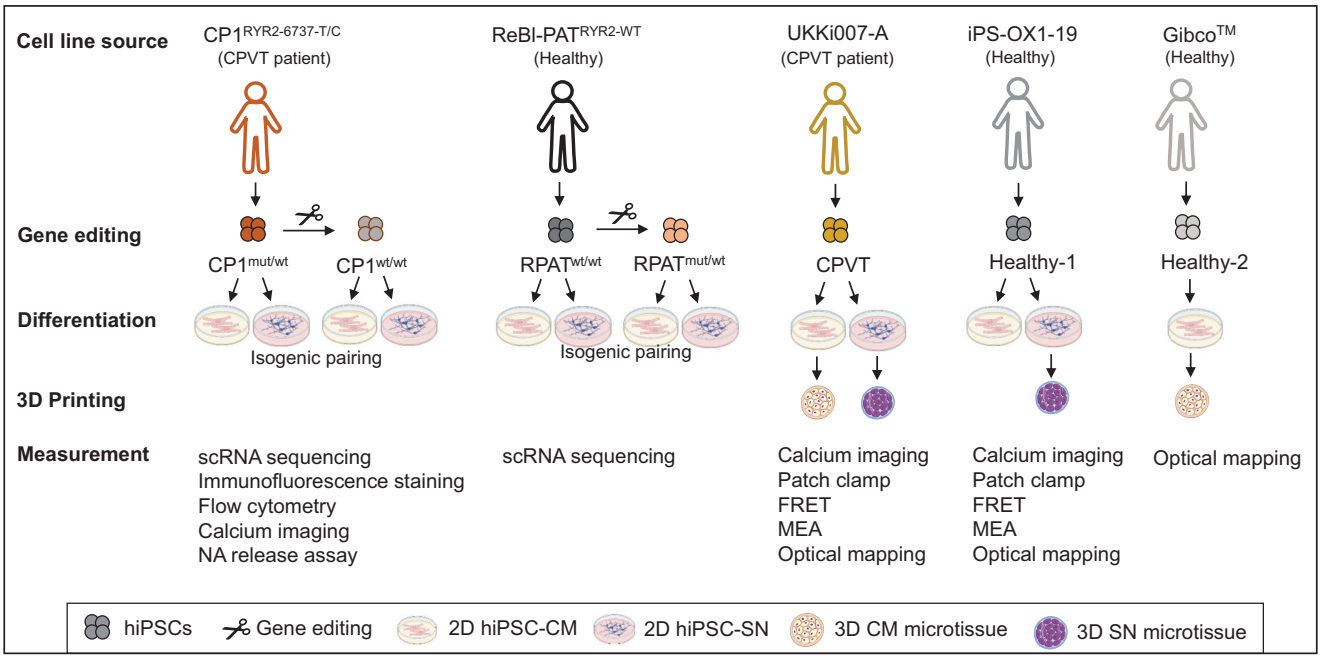

Figure 1. Illustration of study designs
Schematic of experimental strategy using CPVT patient (CP1$^{RYR2\text{-}E737\text{-}T/C}$, UKKi007-A) and healthy control hiPSC lines (ReBl-PAT$^{RYR2\text{-}WT}$, iPS-OX1-19, Gibco^{TM}). Gene editing generated isogenic pairs from CP1 and ReBl-PAT lines to isolate mutation effects. All lines were differentiated into 2D hiPSC-CM and hiPSC-SN, with selected lines used for 3D bioprinted microtissues. Functional characterization employed scRNA sequencing, calcium imaging, patch clamp, FRET measurement, multielectrode arrays, optical mapping, and other molecular assays. CM, cardiac myocytes; CPVT, catecholaminergic polymorphic ventricular tachycardia; FRET, fluorescence resonance energy transfer; hiPSC, human-induced pluripotent stem cells; MEA, multielectrode array; NA, noradrenaline; SN, sympathetic neurons.

(R&D Systems), 10 ng/ml glial cell-line-derived neurotrophic factor (GDNF) (R&D Systems) to promote SN development from Day 4 (Days 4–5: 75% mTeSR+25% N2 medium; Days 6–7: 50% mTeSR+50% N2 medium; Days 8–9: 25% mTeSR+75% N2 medium; Days 11–12: N2 medium]. On Day 12, differentiated cells were detached with Accutase (Thermo Fisher Scientific) and re-seeded on a 24-well plate with a seeding density of 1×10^6 cells/well and cultured in the neuronal medium for 40 days for maturation, after which characterisation and co-culture with iPSC-CMs can be carried out.

3D droplet-printing and microtissue culture

Bioink preparation. Matrigel (Corning, 354234, Loughborough, UK) was used without dilution and thawed at 4°C before use. hiPSC-derived cardiomyocytes or SNs were harvested and dissociated to form a suspension of individual cells. After centrifugation (5 min at 200 *g*), the supernatant was removed. A volume of thawed Matrigel, calculated based on the desired cell-density of 40 million/ml, was then added to the cell pellet. Cells were then suspended in Matrigel on ice to give the bioink for the microfluidic printing process.

Microfluidic fabrication for 3D constructs. The microfluidic platform was improved based on our previous works (Ma et al., 2017; Yang et al., 2023), with new chip design, live droplet imaging and optimised oil conditions. Briefly, a three-dimensional printer (Solid Print3D, Formlabs) was used to fabricate the custom-made reverse mould using clear resin (Formlabs, Somerville, MA, USA). The microfluidic chips were then prepared by casting polydimethylsiloxane (PDMS) on the reverse mould. The PDMS microfluidic chip contains a T junction with a channel size of 600 µm. The two inlets of the microfluidic chip were connected to two syringes that were loaded separately with the prepared bioink and the oil, FC40 (Sigma-Aldrich, F9755). The two inlets were connected and controlled with neMESYS syringe pumps (Cetoni, Korbussen, Germany). Droplets containing cardiomyocytes and Matrigel, separated by the oil, were generated in a polytetrafluoroethylene collection tube with an inner diameter of 600 µm (Cole-Parmer, St Neots, UK). After fabrication, the collection tube was disconnected from the microfluidic chip, sealed with tape, and incubated in a 37°C cell incubator for 2 h. The droplets were then gently flushed out of the collection tube into a 15 ml Falcon tube containing 2 ml of cardiomyocyte culture medium. The 3D cardiomyocyte constructs were then gently transferred with a 1 ml pipette to a 48-well plate containing cardiomyocyte culture medium plus 10 µM Y-27632 Rock inhibitor (Cell Guidance Systems SM02-10, Cambridge, UK) and 100 U/ml penicillin–streptomycin (Thermo Fisher Scientific, 15140122) and maintained at 37°C, 5% CO_2 for the first 24 h. The next day, the medium was exchanged with cardiomyocyte culture medium without additives. A fresh medium change was then performed every 3 days.

Neurocardiac coculture

For 2D monolayer co-culture, contracting hiPSC-CMs over Day 20 and hiPSC-SNs over Day 40 with abundant axon extensions were digested on the same day and reseeded together in Matrigel-coated culture plates for neurocardiac co-culture establishment. hiPSC-CMs were dissociated using TrypLE Express (7–10 min, 37°C, 5% CO_2), while hiPSC-SNs were dissociated using 1 mg/ml collagenase A (Roche, 10103586001, Welwyn Garden City, Hertfordshire, UK) in Hanks' balanced salt solution (20–40 min). Cells were centrifuged, resuspended in a 1:1 mixture of RPMI 1640 and Neurobasal media supplemented with B-27 and N2, and seeded at a 1:1 ratio in a Matrigel-coated plate. The medium was refreshed every other day (Li, Edel et al., 2023). For 3D co-culture, bioprinted 3D cardiac and SN microtissues were co-cultured by placing one cardiac and one neuronal construct into each well of a U-bottom 96-well ultra-low attachment plate. Tissues were maintained in a 1:1 mixture of cardiomyocyte and neuron culture medium to support both cell types. Co-cultures were incubated at 37°C, 5% CO_2, with half-medium changes every 2–3 days. Functional integration was assessed after 7–14 days.

Flow cytometry

Differentiated cells of hiPS cell lines, control ($CP1^{RYR2\text{-}Corr}$) *versus* CPVT ($CP1^{RYR2\text{-}6737\text{-}T/C}$), were collected in a single-cell suspension and centrifuged. Pellets were resuspended and incubated with Live/Dead stain (Thermo Fisher Scientific). Subsequently, the cells were fixed with 4% formaldehyde, permeabilised, and blocked in a blocking buffer. This was followed by incubation with anti-cTnT (MACS 130-120-403, 1:50, Miltenyi Biotec Ltd. Bisley, Surrey, UK) and anti-ventricular myosin light chain-2 (MLC2v, MACS 130-119-581, 1:10) antibodies for hiPSC-CM and anti-tyrosine hydroxylase (TH; Abcam, Cambridge, UK, ab209921, 1:2500) for hiPSC-SN at the required concentrations. Control groups, including dead cell samples, unstained samples and compensation beads (Thermo Fisher Scientific), were prepared. The cells were then resuspended in FACS buffer (phosphate-buffered saline without calcium and magnesium, 2% fetal bovine serum, 0.02% NaN_3) before being run through the flow cytometer (BD Fortessa X20; BD Biosciences, San Jose, CA, USA). The flow cytometer detected the

Table 1. Summary of scRNAseq sample details

Sample id	Genotype	Phenotype	Diagnosis	Target cell type	Cell age at collection
P_011_A11	CP1$^{RYR2\text{-}Corr}$	Control	Edited correction	Cardiac myocyte	Day 41
P_011_D11	CP1$^{RYR2\text{-}6737\text{-}T/C}$	CPVT	CPVT clinical diagnosis	Cardiac myocyte	Day 39
P_011_A10	CP1$^{RYR2\text{-}6737\text{-}T/C}$	CPVT	CPVT clinical diagnosis	Sympathetic neuron	Day 88
P_011_C10	CP1$^{RYR2\text{-}Corr}$	Control	Edited correction	Sympathetic neuron	Day 88
P_011_E10	REBI-PAT$^{RYR2\text{-}WT}$	Control	No clinical symptom	Sympathetic neuron	Day 88
P_011_G10	REBI-PAT$^{RYR2\text{-}13489C/T}$	CPVT	Edited mutation	Sympathetic neuron	Day 88
P_011_B11	CP1$^{RYR2\text{-}Corr}$	Control	Edited correction	Sympathetic neuron	Day 63
P_011_E11	CP1$^{RYR2\text{-}6737\text{-}T/C}$	CPVT	CPVT clinical diagnosis	Sympathetic neuron	Day 66
P_011_B10	CP1$^{RYR2\text{-}6737\text{-}T/C}$	CPVT	CPVT clinical diagnosis	Co-culture	Day 19 (Day 61+ Day 88)
P_011_D10	CP1$^{RYR2\text{-}Corr}$	Control	Edited correction	Co-culture	Day 19 (Day 61+ Day 88)
P_011_F10	REBI-PAT$^{RYR2\text{-}WT}$	Control	No clinical symptom	Co-culture	Day 19 (Day 61+ Day 88)
P_011_H10	REBI-PAT$^{RYR2\text{-}13489C/T}$	CPVT	Edited mutation	Co-culture	Day 19 (Day 61+ Day 88)
P_011_C11	CP1$^{RYR2\text{-}Corr}$	Control	Edited correction	Co-culture	Day 11 (Day 41+ Day 63)
P_011_F11	CP1$^{RYR2\text{-}6737\text{-}T/C}$	CPVT	CPVT clinical diagnosis	Co-culture	Day 11 (Day 39+ Day 66)
QC drop out	CP1$^{RYR2\text{-}6737\text{-}T/C}$	CPVT	CPVT clinical diagnosis	Cardiac myocyte	Day 61
QC drop out	CP1$^{RYR2\text{-}Corr}$	Control	Edited correction	Cardiac myocyte	Day 61

fluorescence of the stained population in the prepared cell samples. Data collected were analysed in FlowJo to report the percentage of cells that expressed tissue-specific markers. The outcomes of double-stained hiPSC-CMs were represented as a density plot featuring a quad gate demarcating positive and negative populations. Single-stained hiPSC-SN data were depicted as a histogram with a ranged gate indicating the negative control region and a bisector gate separating the positive and negative populations.

Single cell RNA sequencing

Two batches of hiPSC-CMs and hiPSC-SNs derived from the two isogenic pairs, CP1$^{RYR2\text{-}6737\text{-}T/C}$ (CPVT) *vs.* CP1$^{RYR2\text{-}Corr}$ (control), and ReBl-PAT$^{RYR2\text{-}13489C/T}$ (CPVT) *vs.* ReBl-PAT$^{RYR2\text{-}WT}$ (control), both in monoculture and co-culture, were prepared for sequencing. Sample details are summarised in Table l.

After dissociation, dead cells were removed using the MACS Dead Cell Removal Kit to improve sample quality. Cell suspensions were centrifuged at 300 *g* for 5 min and resuspended in 100 µl Dead Cell Removal Microbeads (Miltenyi Biotec Ltd. Bisley, Surrey, UK) for 15 min incubation at room temperature. After incubation, cell suspensions were diluted with 500 µl binding buffer and applied to a pre-rinsed MS column, which retained magnetic labelled cell debris, dead cells and dying cells after cell suspension passed through. The column was further rinsed with 2 ml binding buffer. Live cells collected in effluent were centrifuged at 300 *g* for 5 min and resuspended in 1 ml phosphate-buffered saline (PBS) plus 0.04% BSA and transferred to a 2 ml tube for two more washes with centrifugation and resuspension under the same conditions.

Single-cell sequencing libraries were constructed with 10× Genomic (Pleasanton, CA, USA) Chromium Next GEM single cell 3′ reagent kit v3.1 (Dual Index) (16,000–20,000 cell per lane were loaded aiming to recover

Table 2. Summary of the immunofluorescent antibodies

Antibody	Catalogue no.	Dilution	Description
Mouse anti-α-actinin	Sigma A7811	1:800	Myocyte-specific marker
Rabbit anti-cardiac troponin T	ab45932	1.5 µg/ml	Cardiac myocyte-specific marker
Mouse anti-cardiac troponin T	ab8295	1 µg/ml	Cardiac myocyte-specific marker
Mouse anti-tyrosine hydroxylase	Sigma T2928	1:800	Sympathetic neuron marker
Rabbit anti-tyrosine hydroxylase	25859-1-AP	1:200	Sympathetic neuron marker
Rabbit anti-peripherin	ab1530	1:200	Intermediate filament in neurons of the peripheral nervous system
Rabbit anti-synapsin I	ab254349	1:500	Protein regulating neurotransmitter release at synapses
Rabbit anti-PHOX2B	ab183741	1:100	Transcription factor involved in the development of noradrenergic neuron
Alpha-bungarotoxin conjugates	B35450	2 µg/ml	Bind with nicotinic acetylcholine receptor of neuromuscular junction
Mouse anti-SERCA2 ATPase	MA3919	1:100	Calcium pump located in the sarcoplasmic or endoplasmic reticula
Alexa Fluor 488, invitrogen (anti-mouse or -rabbit)	Invitrogen	1:1000	Secondary fluorescent antibody
Alexa Fluor 594, invitrogen (anti-mouse or -rabbit)	Invitrogen	1:800	Secondary fluorescent antibody
Hoechst 33342	H3570	1:10 000	Nucleic acid stain

10 000–12 000 per lane). Prepared sequencing libraries were purified, evaluated the quality using Agilent 4200 Tapestation system (Agilent Technologies, Santa Clara, CA, USA). The final sequencing libraries were sequenced in the Illumina NextSeq 500 system (Illumina, San Diego, CA, USA).

Fastq files were aligned using the 10× Cellranger pipeline (version 6.0.0) aligned to the human genome version GRCh38-2020-A, and quantified using the same pipeline using the default options. Sample normalisation was done in Scanpy (v1.9.2) (10.1186/s13059-017-1382-0), and aggregation and batch correction were done with Harmony (10.1038/s41592-019-0619-0). Leiden graph-clusters were manually annotated by gene markers identified per cluster, independent of model condition. QC filtering, transcripts quantification and differential gene expression assessment under different culture conditions and between healthy and disease genotypes were conducted.

Immunofluorescence imaging

hiPSC-derived D20 CMs and D40 SNs were replated on glass bottom FluoroDish and cultured for 3–5 more days before fixing with 4% formaldehyde. After being permeabilised and blocked in Tris-buffered saline (TBS) plus 0.5% Triton X-100 and 6% donkey serum, cells were incubated with primary antibody diluted in TBS plus 0.1% Triton X-100 and 6% donkey serum (blocking buffer) overnight at 4°C. hiPSC-CMs were stained with anti-cTnT, anti-α-actinin, anti-RyR2 and anti-SERCA2. hiPSC-SNs were stained with anti-TH, anti-PRPH, anti-nAChR, anti-RyR2 and anti-SERCA2 (Table 2). The dish was washed with TBS three times each for 5 min before incubation with secondary antibodies conjugated to Alexa Fluor diluted in blocking buffer at room temperature for 2 h in the dark. Cell nuclei were stained by Hoechst (Thermo Fisher Scientific, H3570) at 1:10 000 dilution in TBS for 10 min. Finally, the dish was washed three times for 5 min again and embedded in Fluoromount aqueous mounting medium (Sigma) to prevent bleaching. Images were taken by Leica confocal microscope (Leica TCS SP5; Leica Microsystems, Wetzlar, Germany) and analysed with LAS X and ImageJ software.

The measurement of sarcomere length involved utilising the cTnT and α-actinin double-stained image, with the distance between two Z lines marked by the anti-α-actinin antibody. Within each cell, three sarcomeres were randomly chosen, and the average of their respective lengths was computed to determine the sarcomere length. Meanwhile, the axonal diameter was determined by assessing the thickness of peripherin-stained neurofilaments. Comparative analysis of sarcomere length and axonal diameter was conducted between disease and healthy cell lines.

Patch clamp

Electrophysiological data acquisition. All electrophysiological data were recorded via a Multiclamp 700B amplifier (Molecular Devices, San Jose, CA, USA) with an Axon Digidata 1550A (Molecular Devices) digitiser. All current clamp recordings were sampled at 10 kHz.

Perfusion. Cells were constantly perfused at a rate of 5–6 ml/min, drugs were applied via this perfusion system. Most drugs were continuously applied for a duration of 5 min before data acquisition; XE-991 and retigabine were perfused for 10 min before recording. Recordings were performed at room temperature.

Whole cell patch-clamp recordings. Whole-cell patch clamp recordings were performed *in situ* on differentiated SNs within the culture dish, without prior enzymatic dissociation, to preserve the native cellular environment and intact neuronal architecture. Whole cell action potential recordings with R values >12 MΩ discarded. Current clamp recordings were bridge-balanced and membrane potentials were corrected for liquid junction potentials. All recordings were monitored throughout, and recordings with RS changes $>20\%$ were discarded. Single action potentials were evoked via a 10 ms positive current injection, at the minimal required injection size. External solution composition was as follows: 135 mM NaCl, 4.5 mM KCl, 20 mM HEPES, 11 mM D-glucose, 1 mM $MgCl_2$, 2 mM $CaCl_2$. External solution pH was adjusted to 7.4 with NaOH. The internal solution was as follows: 130 mM potassium gluconate, 10 mM KCl, 10 mM HEPES, 10 mM sodium phosphocreatine, 4 mM MgATP, 0.3 mM Na_2GTP. Internal pH was adjusted to 7.3 with KOH. 0 mM Mg and 6 mM KCl solution was as follows: 135 mM NaCl, 6 mM KCl, 20 mM HEPES, 11 mM D-glucose, 2 mM $CaCl_2$. The pH was adjusted to 7.4 with NaOH.

Electrophysiological data analysis. Analysis of firing frequency data were performed in Origin 2021 (OriginLab Corp., Northampton, MA, USA). Action potentials were analysed within Clampfit (v10.7, Molecular Devices). Graphs were produced in either GraphPad Prism (v8.2.1; GraphPad Software, San Diego, CA, USA) or Origin 2021 and Adobe Illustrator 2021. Statistical analysis was performed in GraphPad Prism and Origin 2021; all relevant datasets were normality tested.

Firing frequency was taken as the maximum firing rate elicited by a range of 10 pA current injections between 0 and 200 pA. Firing number was taken as the maximum firing number elicited by a range of 10 pA current injections between 0 and 200 pA. Membrane potential was monitored for stability during drug wash-in, and cells with large jumps in membrane potential were discarded.

Action potential parameters were measured from the first step that induced an action potential. Action potential magnitude (mV) was taken as the difference of amplitude between the resting membrane potential and maximum peak response of the action potential. Action potential rise slope (mV/ms) was taken as the maximum velocity from resting membrane potential to the peak amplitude. Action potential decay slope (mV/ms) was taken as the maximum velocity from the peak amplitude to resting membrane potential. Afterhyperpolarisation (AHP) magnitude (mV) was taken as the difference of amplitude between the resting membrane potential and afterhyperpolarisation. Small hyperpolarising pulses were assumed to elicit the least active processes and any points that departed from linearity with these points or contained visible active processes in the final 200 ms of current injection were excluded. Liquid junction potentials were calculated in JPCalcW 50 in Clampex (v11.0.3) (Molecular Devices), where ion availabilities were used instead of concentrations. Whole cell current clamp recordings had an estimated liquid junction potential of −16.9 mV.

Computational modelling

An SN model by Argus et al. (2024) was used to investigate the effects of M-type channel upregulation mathematically and ensure that applying our mathematical understanding of M-current upregulation function could cause equivalent changes in firing rate as the experimental data. The Argus et al. model, as shown in Fig. 6*E*, extends from the model by Tao et al. (2011) to include soma, axon and varicosity regions as well as calcium dynamics that incorporates the endoplasmic reticulum, the bulk soma and the near membrane region. The ion channels included in the model are modelled using Hodgkin–Huxley equations and are detailed in more depth in Argus et al. This model was recalibrated to current clamp data from the CPVT hiPSC-SNs with a genetic algorithm. The parameters that were recalibrated from the Argus et al. model to better match these CPVT neurons were the sodium, leak potassium, A-type potassium, Kv potassium, M-type potassium, BK potassium, SK potassium channel conductances and the voltage kinetics midpoints of the A-type potassium and Kv potassium channel activation gates.

Calcium imaging

Before imaging, cells plated on coverslips were loaded with 5 µM Fura-2AM (Thermo Fisher Scientific) for 30 min at 37°C, then were washed with Tyrode solution (135 mM NaCl, l 4.5 mM KC, 20 mM HEPES, 11 mM glucose, 2 mM $CaCl_2$, us 1 mM $MgCl_2$) three times. Chemical reagents

were dissolved in Tyrode solution and delivered to the cells through a perfusion system with a temperature controller set at 37°C. Flow rate was set at 2–3 ml/min. In the CM monoculture, calcium discharge in response to 0.3 nM, 1 nM isoprenaline, 50 mM KCl and 10 mM caffeine was recorded. Calcium transients in hiPSC-SNs were triggered by 50 mM KCl, 100 μM nicotine and 10 mM caffeine. In the neurocardiac coculture, 50 mM KCl was administered, and cytosolic calcium concentration in hiPSC-SNs was quantified. The region of interest (ROI) for fluorescence intensity capture was selected based on microscopic features. Image acquisition was performed at 340 and 380 nm excitation using a QICLICK digital CCD Photometrics (QImaging, Surrey, UK) camera connected to an OptoLED fluorescence imaging system, which was housed on a Nikon (Amstelveen, The Netherlands) eclipse Ti2 inverted microscope equipped with a ×40 oil immersion objective. Background intensity was subtracted from emission intensity for both excitation wavelengths for each image, then calcium concentration was calculated as the 340 nm/380 nm ratio, and the change of calcium concentration was normalised to the baseline ratio for comparison among groups.

Fluorescence resonance energy transfer

Cells were prepared as a monolayer on coverslips, transfected with adenoviral vectors encoding the fluorescence resonance energy transfer (FRET) cAMP sensor Epac-S^{H187} by overnight incubation at 37°C, 5% CO_2 before FRET measurements. Viral volume was adjusted by cell amount. After transfection, cells were allowed to replicate and express the FRET sensor for 2–3 days. cAMP generation was induced using 100 nM isoprenaline for hiPSC-CM, 200 μM nicotine for hiPSC-SN and saturated using 25 μM foskolin plus 100 μM 3-isobutyl-1-methylxanthine (IBMX). The cells were either perfused or bathed in Tyrode solution to reach a steady state before chemical agents were applied to the cells by diluting them in Tyrode solution. During the process, images were taken using a Nikon Eclipse Ti2 inverted microscope with a ×40, oil immersion objective, connected to a Cairn Research (Kent, UK) Ltd dual OptoLED light source and a Prisme-BSI photometric camera. Cells were excited every 15 s for 100 ms; the excitation wavelength was set at 430 nm, and emission intensities were recorded at 480 nm for cyan fluorescent protein (CFP) and 535 nm for yellow fluorescent protein (YFP). Background fluorescence was subtracted from the recorded emission intensities, and the raw FRET ratio was calculated as recorded CFP emission intensities over YFP emission intensities. Peak values following drug stimulation were compared across groups. For comparison, the raw ratio was normalised to the average ratio at baseline (R0) and the drug effect on FRET change was represented as a percentage to the saturated cAMP level.

Electrical mapping

Microelectrode array (MappingLab EGMA064200700, Oxford, UK) was pre-coated sequentially with 0.1% polyethyleneimine and Matrigel. Mature hiPSC-CMs were digested by TryPLE with 7 min of incubation at 37°C, 5% CO_2. Detached myocytes were then collected and centrifuged at 300 *g*, 4 min, and resuspended in RB+ medium at a concentration of 5×10^6/ml. Myocytes were replated on a microelectrode array (MEA) by adding 40 μl of cell suspension covering the electrode area. Medium (RB+ supplemented with 10 μM Rock inhibitor Y-27632) was slowly topped up to 1 ml after 2 h of incubation that allowed cell attachment. In neurocardiac co-culture array, Days 40–60 hiPSC-SNs were digested using Accutase, mixed with hiPSC-CMs suspension at 2:3 ratio, for re-plating on the microelectrode. Myocytes were recovered after reseeding for 3–5 days, and the culture medium was changed every other day. Experiments were conducted when CMs regained spontaneous contraction. Microelectrode with attached CMs was installed onto the electrical mapping machine (MappingLab cat. no. 16-1036CS) that records the electrical field signals of CMs simultaneously from 64 channels. In the monoculture set-up, baseline and 1 μM isoprenaline-stimulated field potentials were recorded. The co-culture system was subjected to stimulation by 100 μM nicotine to replicate the accelerated heart rate induced by activated SNs. EMapRecord 5 acquisition software was employed for the recording of electrical signals, and subsequent analysis was conducted using EMapScope 5. Parameters assessed encompassed field potential duration (FPD, Bazett's correction: $FPDcB = FPD/RR^{1/2}$), RR interval, the width of the QRS complex (depolarisation duration), the width of the T wave and conduction velocity.

Optical mapping

High-resolution optical mapping was conducted using an Optical Mapping System (MappingLab). 3D monocultured or co-cultured microtissues were incubated in a culture medium containing Rhod-2 AM (10 μM, Abcam, ab142780) and Pluronic F127 (0.042%, Thermo Fisher Scientific, P3000MP) at 37°C with 5% CO_2 for 30 min. Following a single wash with Tyrode's solution, the cells were incubated in Tyrode's solution containing blebbistatin (10 μM, Abcam, ab120425) for 15 min. The stained microtissues were placed in a 35 mm Petri dish on a heated stage, with the solution temperature maintained at 34 ± 0.5°C. Excitation light was applied using two 530

± 25 nm LEDs, filtered through a 550 nm long-pass filter (LEDC-2001, MappingLab). Emitted fluorescence was collected through an objective lens and filtered with a 590 nm band-pass filter (35 nm bandwidth) to detect Ca^{2+} signals. Signals were recorded using a high-speed CMOS camera (OMS-PCIE-2002, MappingLab), capturing both baseline activity and responses to 100 nM isoprenaline stimulation. Data acquisition was performed with OMapRecord 5 software, while subsequent analysis was conducted with OMapScope 5. For signal processing, Gaussian spatial filtering (3 × 3 pixels) and zero-phase median filtering were applied. Analysed parameters included beat rate, conduction velocity, active time, amplitude and calcium transient duration.

Noradrenaline release assay

Noradrenaline (NA) concentrations in neuronal culture medium were measured using an enzyme-linked immunosorbent assay (ELISA) kit (Abcam ab287789) following the manufacturer's instructions. Control and CPVT hiPSC-SNs were re-plated on a 24-well plate at 1 million per well on Day 12 and fed until Day 40. To collect supernatant for ELISA, cells were treated with 1 ml plain neuronal media or neuronal medium supplemented with 100 µM nicotine for 1 h. Collected samples were added in duplicate to 96-well plated supplied in the NA-release ELISA kit and incubated with biotin, streptavidin–horseradish peroxidase (HRP) conjugate and TMB (Tetramethylbenzidine) substrate sequentially. Then optical density for absorbance was measured at 450 nm and NA concentration in supernatant was calculated from the standard curve.

Measurement of noradrenaline from single cells using fast scanning cyclic voltammetry

Commercially available 5 µm carbon fibres were utilised to measure evoked release of NA as previously described (Wolf et al., 2016) with the modification of scan rate, which was set to 12 V/s. Cultured hiPSC-SNs from either control patients or patients with CPVT were placed on the stage of an inverted microscope and a 5 µm-diameter insulated carbon fibre electrode was placed near the soma of the cells. The command potential of the electrode was cycled between −500 and 1200 mV to span the oxidation and reduction potentials of NA. Currents were measured at the peak oxidation potential and provide the magnitude of NA release. The integral of the oxidation current provides total NA release. Cells were superfused with Tris-buffered saline of the following composition: 40 mM Tris base, 132 mM NaCl, 4.2 mM KCl, 11.2 mM glucose, 2 mM $CaCl_2$, 0.7 mM $MgCl_2$. Recordings were initiated and baseline recorded for 180 s. At the 180 s time point, 200 µl elevated K+TRIS buffer (700 mM KCl) was added to bring the total bath volume to ∼50 mM K^+. Data were filtered 700–1000 Hz and digitised at 10 kHz.

Statistical analysis

Before conducting Student's *t* test and the ANOVA test, all data underwent an assessment for normal distribution and homogeneity of variance. In cases where the data did not exhibit normal distribution, non-parametric tests, such as the Mann–Whitney test for *t* tests and the Kruskal–Wallis test for ANOVA, were employed. Welch's correction was applied to the *t* test or the ANOVA test in cases of unequal variances. All data were presented as means ± SD. Data analysis and plotting were performed using GraphPad Prism; figures were created using BioRender.

For single cell RNA sequencing, for every gene within each pathway, normalised expression values were compared between groups (CPVT *vs*. control) using a two-sided Mann–Whitney *U* test. For each comparison, we computed the log-fold change (log2FC), *Z*-score, and raw *P*-value, followed by Benjamini–Hochberg false discovery rate (FDR) correction across all tested genes to control for multiple testing. Reported significance levels and annotations in the figures correspond to the FDR-adjusted *P*-values. Expression distributions were visualised as per-gene single-cell points, faceted by pathway. Each subplot displays group-specific distributions and associated significance markers ($^{*}P < 0.01$, $^{**}P < 0.0001$, $^{***}P < 10^{-6}$, n.s., non-significant).

Results

hiPSC differentiated cardiac myocytes and sympathetic neurons expressed cell-type-specific markers

To validate the induction efficiency of hiPSC-CM and hiPSC-SN, the expression of tissue specific markers was explored using flow cytometry. More than 80% of differentiated myocytes were double positive for cardiac troponin T (cTnT) and myosin light chain 2v (MLC2v), which suggested these cells were ventricular CMs in nature (Fig. 2*A*). Tyrosine hydroxylase (TH) positive neurons accounted for 80–90% of differentiated cells among the cell lines (Fig. 2*B*).

To further reveal the cellular heterogeneity and explore the regulatory changes in triggered arrhythmia, we performed single cell RNA sequencing (scRNAseq) on the CMs and SNs differentiated from CPVT hiPSCs and normal hiPSCs. After dead cell removal and quality control filtering, two CM samples, six SN samples and six neurocardiac 2D co-culture samples were included in the run, with half from CPVT hiPSCs and half control.

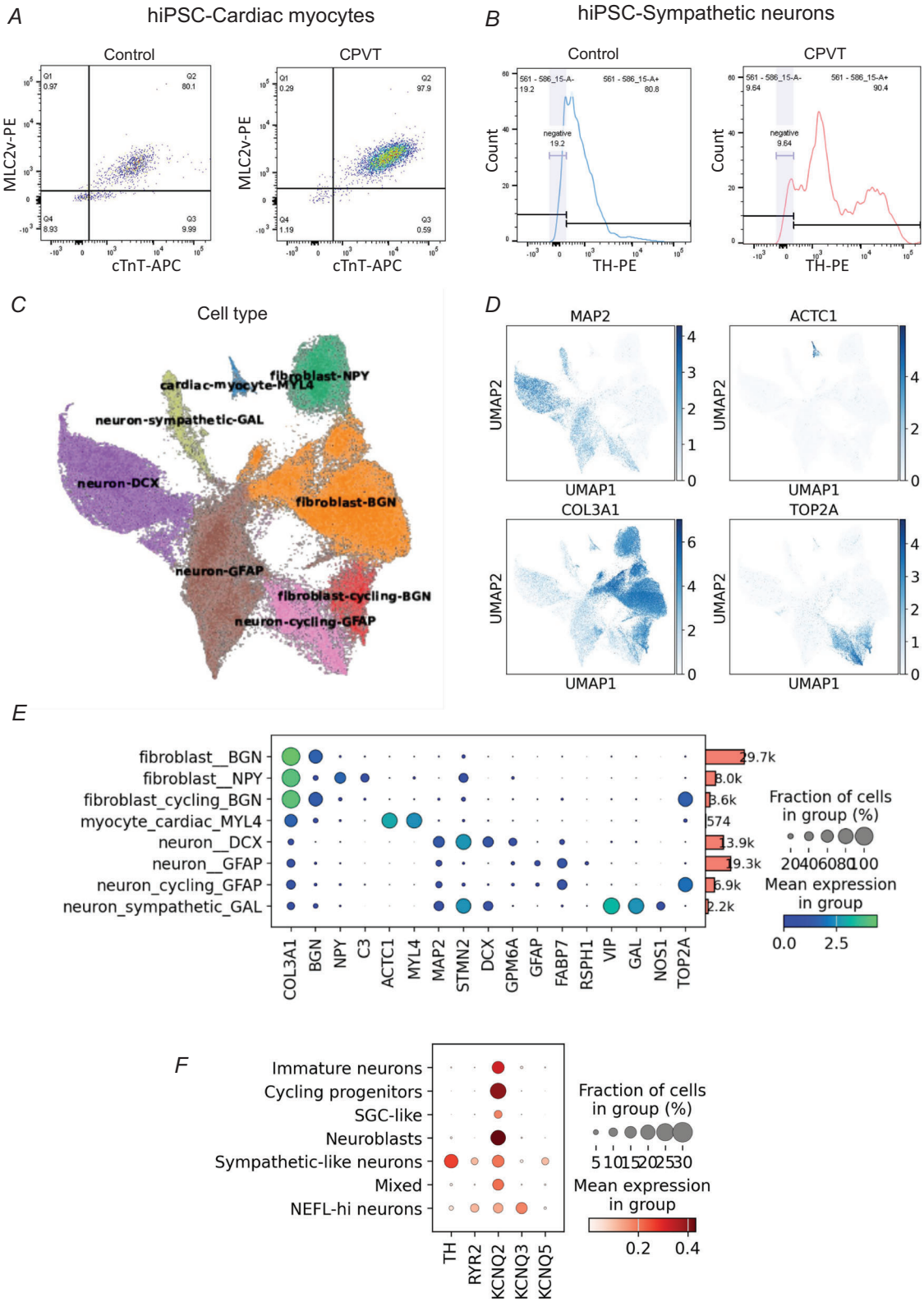

Figure 2. Cell-specific marker profiles of hiPSC cardiac myocytes and sympathetic neurons
A, flow cytometry of hiPSC cardiac myocytes. A two-parameter density plot was employed to visualise the stained population in hiPSC-CM samples derived from CPVT cell lines, CP1$^{RYR2\text{-}6737\text{-}T/C}$ and an isogenic control cell lines CP1$^{RYR2\text{-}Corr}$. The right-upper quadrant (Q2) of the density plot specifically delineated the MLC2v and cTnT double-positive populations, which were 80.1% in the control line and 97.9% in the CPVT line. *B*, flow cytometry

of hiPSC sympathetic neurons. The expression of cell type-specific markers in sympathetic neurons was examined within the context of CPVT ($CP1^{RYR2\text{-}6737\text{-}T/C}$) *versus* control genotypes ($CP1^{RYR2\text{-}Corr}$). The histogram depicted TH^+ neurons as 80.8% in the control line and 90.4% in the CPVT line. *C*, UMAP visualisation of cell clusters generated from the combination of the single RNA sequencing gene profile of hiPSC-derived cardiac myocytes, sympathetic neurons and neurocardiac co-culture samples. *D*, expression of *MAP2* (microtubule-associated protein 2), *ACTC1* (actin alpha cardiac muscle 1) and *COL3A1* (collagen type III alpha 1 chain) revealed three major cell types of the differentiation as neuron, myocyte and fibroblast, respectively. *TOP2A* encoding for DNA topoisomerase II involved in transcription expressed highly in a labile cell population. *E*, key marker genes used for subpopulation identification. *GAL*, *VIP* and *NOS1* were primarily expressed in sympathetic neurons; *ACTC1* and *MYL4* were primarily expressed in cardiac myocytes. *F*, presence of *TH*, *RYR2*, *KCNQ2/3/5* gene in hiPSC-sympathetic neurons.

Leiden clustering of the scRNA-seq data, following batch correction and uniform manifold approximation and projection (UMAP), revealed eight cell clusters (Fig. 2*C*), which aligned to three major cell populations, namely neurons, CMs and fibroblasts, indicated by enriched known cell type markers *MAP2*, *ACTC1* and *COL3A* as illustrated in Fig. 2*D*. *TOP2A* expressed in a neuron and a fibroblast cluster indicated labile cells under active division. Cell populations were further classified according to top-ranked expressed genes within each cluster (Fig. 2*E*). CMs and SNs were both confirmed by exclusively enriched marker genes expressed in the cluster, namely *ACTC1* and *MYL4* in CMs, and *GAL*, *VIP* and *NOS1* in SNs. In addition, expression of *TH*, *RYR2* and *KCNQ2/3/5* genes was present in SNs (Fig. 2*F*).

Morphological disparities between genotypes were insignificant

For the identification of the morphological disparities between CPVT and normal cell lines, prepared cell-culture monolayer were stained with immunofluorescence antibodies specific to SNs and CMs. The extension of neurites from TH positive SNs was outlined by antibody targeting peripherin (PRPH) (Fig. 3*A*). To quantitatively assess anatomical features, axonal diameter for SNs were measured; no significant difference was detected between the isogenic control (0.592 ± 0.150 µm, $n = 68$ cells in 7 coverslips) and CPVT neurons (0.581 ± 0.138 µm, $n = 51$ cells in 4 coverslips, Mann–Whitney test, $P = 0.8129$, Fig. 3*B*). We also detected the expression of nicotinic acetylcholine receptors (nAchR) in the SN body (Fig. 3*C*), along the axon and at the synapse using α-bungarotoxin conjugates. These acetylcholine receptors indicated the structural basis of hiPSC-neurons to be activated by upstream chemical stimulation from related cells and external chemical reagents application. As the pathogenic mutation in CPVT mainly alters the function of the ryanodine receptor, the subcellular localisation of RyR was identified in the sarcoplasmic reticulum using anti-RyR2 and anti-SERCA2 in neurons, after confirming its expression when co-stained with anti-TH in the neuron (Fig. 3*D* and *E*). This colocalisation was not well exhibited in the neuron, possibly due to the large nucleus-to-cytosol ratio of the neuron, the resolution limit and that the neuron has an endoplasmic reticulum, being a neurosecretory cell. To visualise sarcomere organisation, hiPSC-CMs were stained with anti-cTnT and anti-α-actinin (Fig. 3*F*). Organised sarcomeres were visualised in both CPVT and control CMs, and sarcomere length showed no significant differences between CPVT (2.047 ± 0.187 µm, $n = 27$ cells in 16 slices) and control groups (2.065 ± 0.194 µm, $n = 34$ cells in 12 slices, *t* test, $P = 0.722$, Fig. 3*G*). RyR2 was also identified in the sarcoplasmic reticulum using anti-RyR2 and anti-SERCA2 antibodies in hiPSC-CMs (Fig. 3*H* and *I*), with co-staining using anti-α-actinin (Fig. 3*H*). The sheet-like structure of the sarcoplasmic reticulum was clearly displayed in the CMs, with RyR2 expression superimposed on these sheets. At the resolution limit of the confocal microscope, no discernible differences were observed in the expression and assembly of these critical functional and structural proteins within myocytes and neurons across genotypes.

CPVT sympathetic neuron demonstrated hyperactive responses

Electrophysiological property. To test the membrane excitability of SNs differentiated from hiPSCs, these cells were subjected to electrical stimulation during disrupted ion homeostasis due to patch clamp interrogation with a non-physiological extracellular solution. We measured the firing frequency and firing number at rheobase using the patch clamp technique to compare the neuronal excitability between CPVT and control. Whole-cell patch-clamp measurements demonstrated that SNs derived from CPVT hiPSCs had a significantly higher firing frequency than neurons from healthy hiPSC lines (Fig. 4*A* and *B*). The firing number at rheobase (minimal current injection of duration >300 ms required to reach the action potential threshold) was also significantly higher in CPVT neurons (Mann–Whitney *U* test; $P = 0.0339$) when measured by a series of 10 pA current steps of duration 500 ms in the range 0–200 pA in amplitude.

Neuronal firing behaviour was classified into three firing properties according to previous work (Cassell et al., 1986). Phasic 1 firing neurons represent neurons that

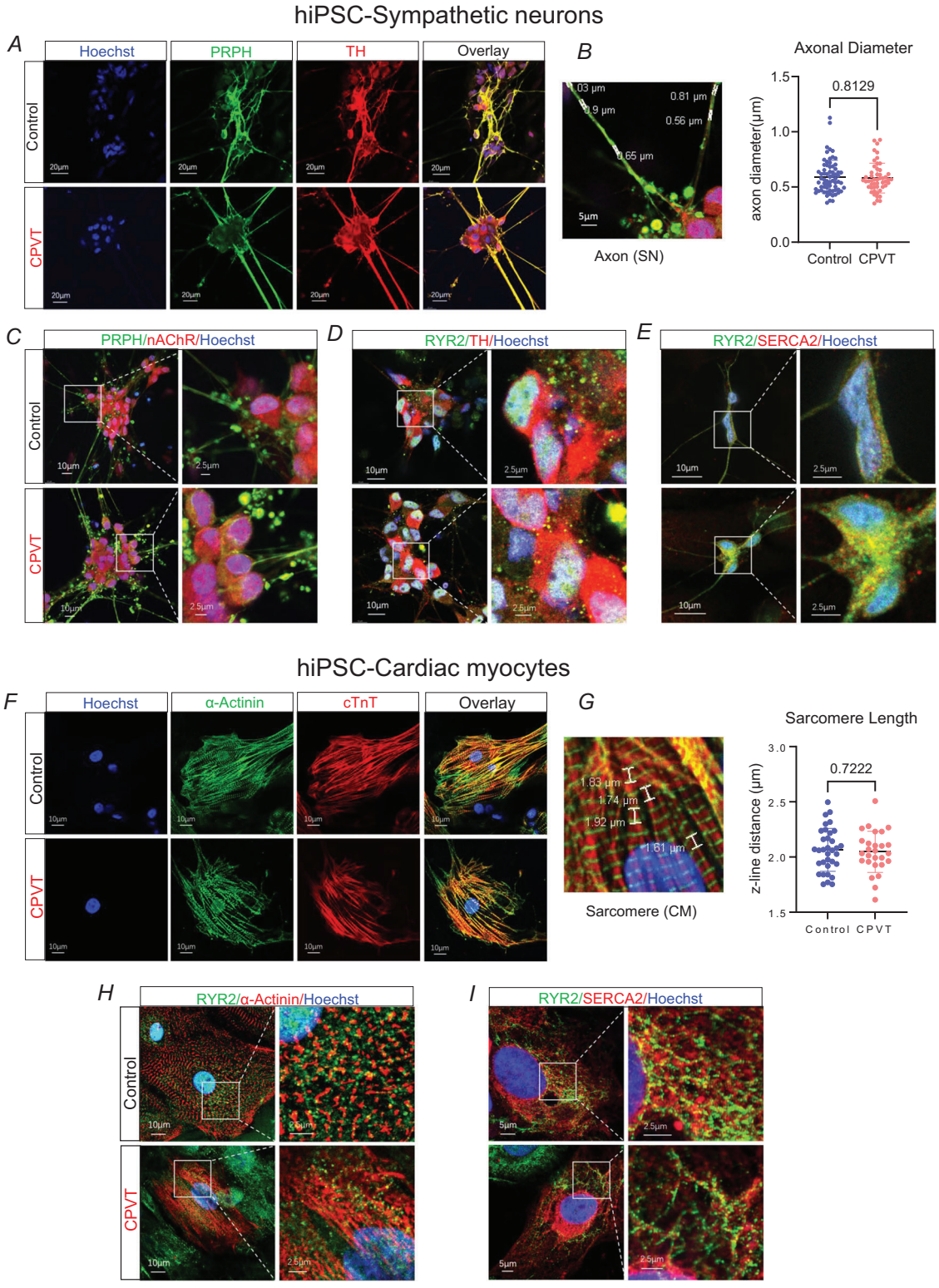

Figure 3. Immunofluorescence staining for the structural and functional proteins in hiPSC-sympathetic neurons and cardiac myocytes
Cells derived from a CPVT cell line, CP1$^{RYR2\text{-}6737\text{-}T/C}$, and an isogenic control cell line, CP1$^{RYR2\text{-}Corr}$. *A*, double staining with TH and peripherin validated the cells as dopaminergic neurons in the peripheral nervous system. *B*, axonal diameter was measured in peripherin-stained hiPSC-SNs. *C–E*, these neurons also expressed nicotinic acetyl-

choline receptors (*C*) and RyR2 receptors in the cell body (*D*), which co-stained with the endoplasmic reticulum marker SERCA2 (*E*). *F*, cTnT and α-actinin staining showed the well-organised myofibrils and contractile unit sarcomere. *G*, sarcomere length was measured as the distance between 2 consecutive α-actinin stained lines. *H* and *I*, RyR2 expressed in α-actinin positive cells in the cytoplasm (*H*) colocalised with SERCA2, which outlines the sarcoplasmic reticulum as a continuous linear-shaped structure spread out from the nucleus (*I*).

fire only one action potential during a 500 ms current injection in the range of 0–200 pA. Phasic 2 firing neurons fire 2–5 action potentials, all within the 500 ms stimulation pulse for all recordings within the stimulation range 0–200 pA. Tonic firing neurons fire >6 action potentials within the current injection range 0–200 pA. CPVT hiPSC neurons were found to be predominantly tonic firing, while control neurons comprised a higher percentage of tonic 1 and tonic 2 firing neurons (Fig. 4*C*).

Calcium transient, cAMP signalling and neurotransmitter release. Calcium is critical for neurotransmission and was measured using Fura-2AM calcium indicator in CPVT and healthy hiPSC-neurons. Similar to membrane excitability, SNs derived from the CPVT cell line ($CP1^{RYR2\text{-}6737\text{-}T/C}$) had markedly enhanced intracellular Ca^{2+} transients compared to its isogenic control during stimulation by either 100 μM nicotine (CPVT 1.571 ± 1.247, $n = 33$, *vs.* control 0.466 ± 0.566, $n = 32$, Mann–Whitney test $P < 0.0001$), 10 mM caffeine (CPVT 0.650 ± 0.482, $n = 113$, *vs.* Con-1 0.276 ± 0.141, $n = 43$, *vs.* Con-2 0.351 ± 0.298, $n = 37$, Kruskal–Wallis test, $P < 0.0001$) or 50 mM KCl (CPVT 2.594 ± 2.011, $n = 33$, *vs.* control 1.31 ± 1.228, $n = 32$, Mann–Whitney test $P < 0.0001$) as shown in Fig. 4*D* and *E*. These chemical reagents examined calcium responses from different origins. Application of nicotine mimics chemical neurotransmitters released from input neurons at the synapse, which act on the acetylcholine receptor on the post-synaptic membrane that facilitates calcium influx. Caffeine induces calcium release from the endoplasmic reticulum (ER) through ryanodine receptors, possibly by modulating the opening threshold of the ryanodine receptor to the calcium concentration (Rojo-Ruiz et al., 2018). High potassium depolarises the neuron and triggers the opening of the voltage-gated calcium channels.

cAMP–protein kinase A (PKA) phosphorylation is one of the post-translational modifications of RyR2 receptors that control the release of Ca^{2+} from intracellular stores. Using the FRET technique, the cAMP sensor Epac-S^{H187} was transduced to hiPSC-SNs 48 h prior to 200 μM nicotinic stimulation. CPVT hiPSC-SNs demonstrated a significantly higher increase in cAMP levels compared to control hiPSC-SNs. Cells were then exposed to a saturation dose of 100 μM IBMX + 25 μM forskolin (FSK) to demonstrate the FRET probe was still in the dynamic sensing range (Fig. 4*F*).

We then tested whether neurons could release NA, the main neurotransmitter in SNs. Two methods were employed, an ELISA assay and fast scanning cyclic voltammetry (FSCV). First, supernatants from hiPSC-SNs were collected both at baseline and after nicotine stimulation for the quantification of NA concentration. In control neurons, the baseline NA concentration in the supernatant was 108.3 ± 19.19 pg/ml, rising to 149.0 ± 33.44 pg/ml post-stimulation. In contrast, the baseline and stimulated NA concentrations in the CPVT neuron supernatant trended upwards compared to control, measuring 151.7 ± 35.57 and 171.3 ± 27.11 pg/ml, respectively (Fig. 4*G*), although these differences were not statistically significant, which might be related to the one time domain measurement. To overcome this, we next measured and compared NA levels in cultured hiPSC-SNs derived from either control patients or patients with CPVT, employing FSCV in a time-resolved manner (Fig. 4*H*). Basal NA currents were slightly elevated in CPVT compared to control cells (0.13 ± 0.34 nC versus −0.19 ± 0.82 nC, respectively), but there was no statistical difference. Both control and CPVT neurons exhibited robust NA release with elevated potassium stimulation with control cells releasing 43.71 ± 42.74 nC and CPVT cells releasing 36.74 ± 56.90 nC, but the enhanced calcium phenotype did not phenocopy to a statistical difference in neurotransmission (Fig. 4*I*–*K*). This might be related to the sample size of 16 for each data set and/or the developmental state of the cells.

CPVT cardiac myocytes characteristics

CPVT hiPSC-CMs exhibited irregular rhythm. To characterise the features of the baseline cardiac action potential, microelectrode array measurements were conducted on Day 37 from normal and diseased hiPSC-derived CMs (Fig. 5*A*). At baseline, 47% (8 out of 17) of CPVT hiPSC-CMs demonstrated arrhythmic properties in their spontaneous beating, including tachycardia and re-entry phenomena, while none of the control myocytes exhibited irregular rhythm. Among the regular beating myocytes, CPVT myocytes exhibited shortened RR intervals and field potential duration (Fig. 5*B*). Application of isoprenaline (β-adrenergic stimulation) induced a significant increase in heart rate for both control and CPVT cell lines, although it is worth noting that no arrhythmias were triggered by 100 nM isoprenaline (Fig. 5*C*).

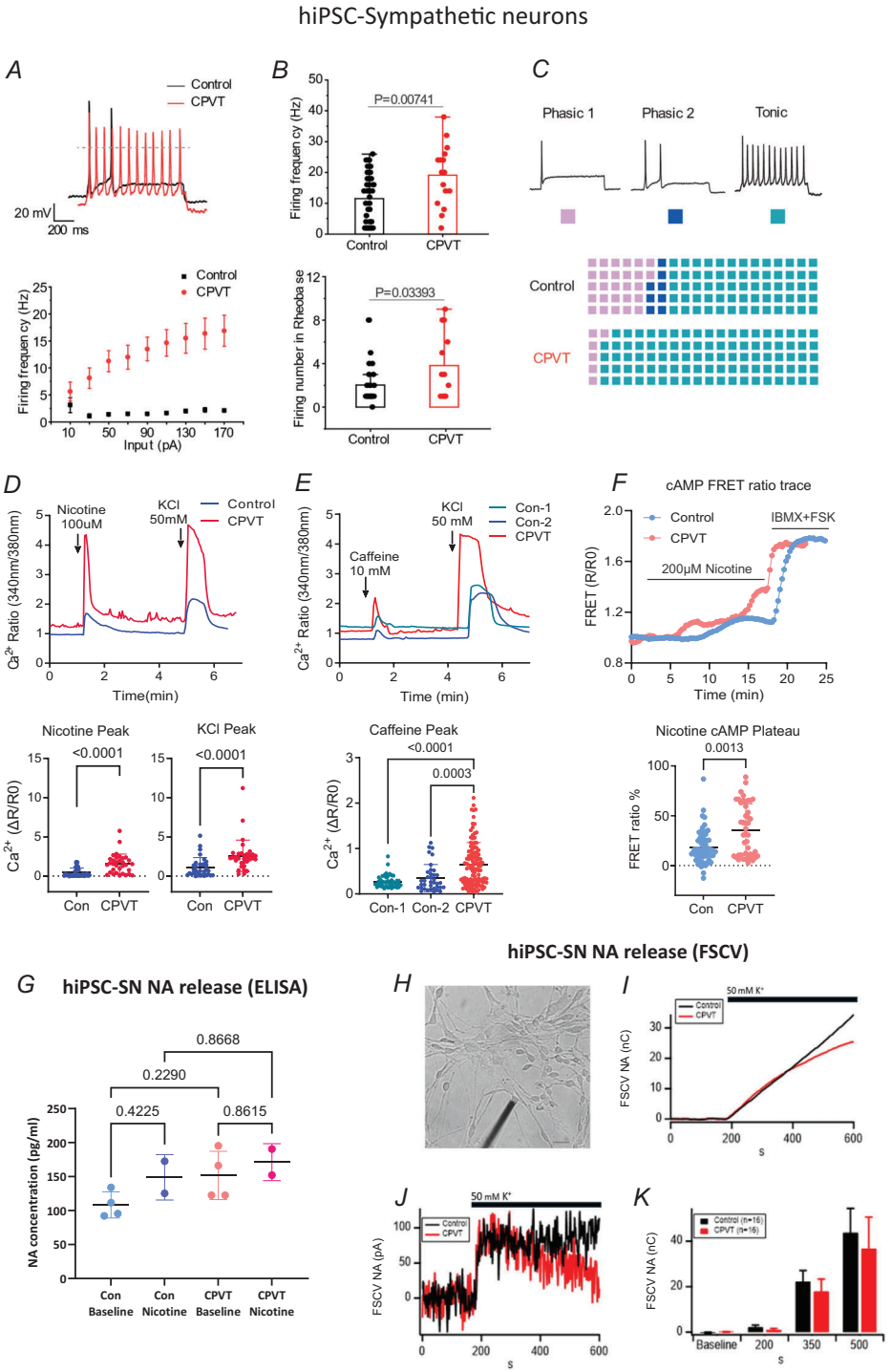

Figure 4. Functional phenotypes of CPVT versus healthy hiPSC-sympathetic neurons
A, spontaneous firing frequency of CPVT neurons was higher than control neurons at all tested current amplitudes. *B*, firing frequency and firing number of CPVT neurons and control neurons. *C*, examples of neuronal firing behaviour subtypes, including phasic 1, phasic 2 and tonic firing, indicated by a coloured square. A trend towards tonic firing neurons was discovered in CPVT neurons. Control neurons: phasic 1 n = 13, phasic 2 n = 9, tonic n = 27; CPVT neurons: phasic 1 n = 1, phasic 2 n = 3 tonic n = 12. *D* and *E*, representative Ca^{2+} dynamics trace in hiPSC-SN monoculture in response to 100 μM nicotine and 50 mM KCl (CPVT n = 33 cells in 2 coverslips, isogenic control n = 32 cells in 2 coverslips) and 10 mM caffeine [non-isogenic control (Con-1) n = 43 cells in 5 coverslips, isogenic control (Con-2) n = 37 cells in 5 coverslips, CPVT n = 113 cells in 11 coverslips]. *F*, FRET ratio trace of acetylcholine receptor stimulation triggered cytosolic cAMP. The maximal increase of cAMP level was significantly higher in CPVT neurons (35.80% ± 25.97%, n = 45 in 4 coverslips) compared to non-isogenic

control neurons (18.06% ± 16.39%, *n* = 63 in 4 coverslips) (Mann–Whitney test, *P* = 0.0013). *G,* noradrenaline (NA) release assay using ELISA kit. Both baseline and nicotine-stimulated NA release were found to be higher in CPVT ($CP1^{RYR2\text{-}6737\text{-}T/C}$) compare with control neurons ($CP1^{RYR2\text{-}Corr}$), although not reaching statistical significance. Notably, hiPSC-SNs demonstrated responsiveness to nicotine stimulation, resulting in an elevation of NA secretion in both Con and CPVT cell lines. *H-K,* noradrenaline release from hiPSC-SN using fast scanning cyclic voltammetry (FSCV). *H,* a micrograph of the seeded hiPSC-SN. A 5 µm carbon fibre can be seen near a body of one of the cells. Scale bar = 20 µm. *I,* Representative raw records are provided for control and CPVT cells. *J,* the raw records in panel *I* were integrated to generate cumulative NA release, shown in the plots. *K,* data were pooled from all records and are presented as mean ± SD.

Uncoordinated calcium release and enhanced cAMP response were detected in CPVT CMs. Calcium imaging demonstrated enhanced intracellular calcium transients in CPVT hiPSC-CMs. Application of either isoprenaline, or KCl (membrane depolarisation) or caffeine (RyR2 receptor activator) raised the Ca^{2+} transient in healthy and CPVT myocytes, with the diseased myocytes presenting irregular spontaneous calcium discharges after stimulation (Fig. 5*D* and *E*). This extra calcium release would predispose to the well-established afterdepolarisations seen in CPVT (Schneider et al., 2025). Moreover, the isoprenaline-triggered calcium increase was significantly higher in CPVT myocytes (0.99 ± 0.498, $n = 14$ cells in 2 coverslips) compared to healthy myocytes (0.05 ± 0.031, $n = 11$ cells in 2 coverslips), Welch's *t* test, $P < 0.0001$. Although the size of the calcium transient in response to KCl and caffeine was not statistically different in CPVT myocytes when compared to healthy myocytes, irregular calcium discharge was detected in 24 out of 31 (77.4%) diseased myocytes, whereas only 1 out of 10 (10%) healthy myocytes presented spontaneous calcium discharge (Fig. 5*D* and *E*).

To determine whether CPVT hiPSC-CMs have elevated cAMP levels compared to control hiPSC-CMs, FRET experiments were performed. hiPSC-CMs transfected with cAMP sensor Epac-SH187 were exposed to 100 nM isoprenaline to stimulate cAMP production and 100 µM IBMX + 25 µM FSK to saturate the FRET sensor. For comparison, the raw ratio was normalised to the average ratio at baseline (R0) and the drug effect on the FRET change was represented as a percentage change to the saturated cAMP level. The change in FRET ratio, which represents the elevation of cAMP levels in response to 100 nM isoprenaline, was found to be significantly higher in CPVT hiPSC-CMs compared to the control (Fig. 5*F*, control: 48.63 ± 16.08%, $n = 98$; *vs.* CPVT: 64.25 ± 16.65%, $n = 70$; Mann–Whitney test; $P < 0.0001$).

Modulation of M-current altered the electrophysiological excitability of hiPSC sympathetic neurons

Increased expression of *KCNQ2/3* and downregulation of the channel was observed in CPVT neurons (Fig. 3), which is known to be associated with epilepsy (Iftimovici et al., 2023). The M-current (I_M) inhibitor XE-991 (10 µM) and activator retigabine (3 µM) were used to assess the role of this current in regulating the electrophysiological excitability in control and CPVT hiPSC SNs. I_M inhibition induced spontaneous action potential firing in 9 out of 10 inert control neurons (Fig. 6*A*) and reduced the rheobase within a stimulation range of 10–200 pA (from 129 ± 13 to 83 ± 15 pA, $P = 0.00113$) (Fig. 6*C*). Since CPVT neurons presented higher spontaneous firing rate, increasing I_M via the activator retigabine was also tested to evaluate whether it would be sufficient to reduce CPVT neuronal excitability. Application of retigabine reduced the spontaneous firing rate in all CPVT tonic firing neurons (Fig. 6*B*). I_M activation also increased the rheobase amplitude in CPVT neurons that fired within 10–90 pA stimulations (from 12 ± 4 to 73 ± 6 pA, $P = 0.00005$) (Fig. 6*D*). Moreover, the behaviour of the neuron could be reconstructed and mimicked using computational modelling by altering M-current parameters (Fig. 6*E*). In particular, Fig. 6*F* illustrates the model closely resembles the experimental results (Fig. 6*D*, middle) over input stimulation currents of 10–70 pA. Additionally, upregulating M-current conductivity from 2.3 to 4 nS (Fig. 6*G*) showed comparable results to retigabine (M-current activator) in reducing the excitability of neurons.

Neurocardiac interaction in 2D co-culture

Cell type-specific marker staining in neurocardiac co-cultures confirmed the presence of CMs (cTnT) and SNs (TH) reseeded together (Fig. 7*A*). To ascertain potential distinctions in the impact of control and CPVT myocytes on SNs, calcium transients in neurons were measured in the co-culture (myocyte and neuron of same genotype) and cross-culture (myocyte and neuron of different genotype) set-ups (Fig. 7*B*). High potassium was introduced to the neurocardiac co-culture, leading to depolarisation of the plasma membrane in both myocytes and neurons. Fura-2 fluorescence intensity, measured from SNs, revealed that CPVT neurons exhibited a higher amplitude of calcium transients, irrespective of whether they were in coculture or cross-culture. Interestingly, within the same genotype, the amplitude of neuro-

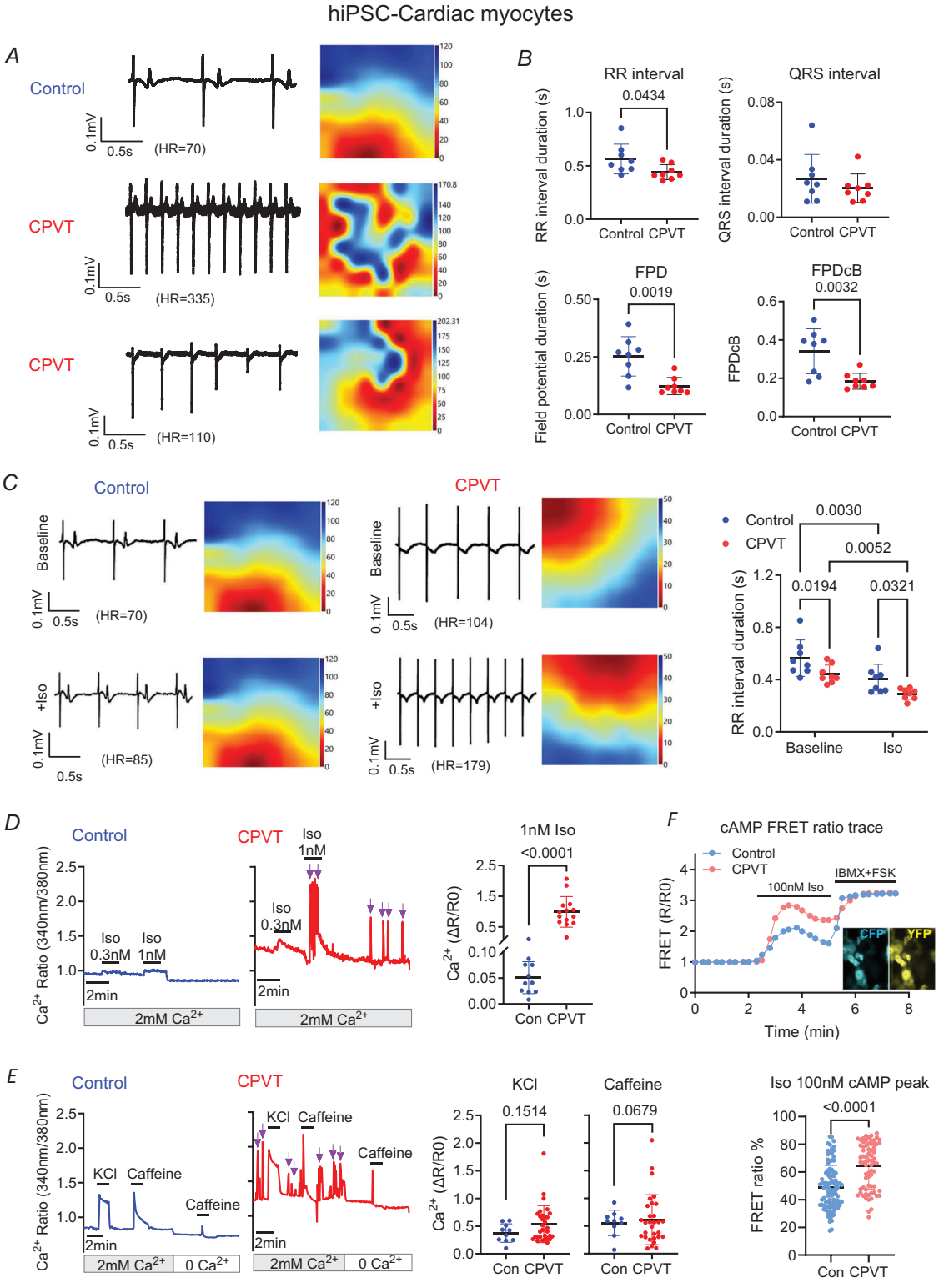

Figure 5. Functional phenotypes of CPVT versus healthy hiPSC-cardiac myocytes
A, example baseline field potential traces in control and CPVT hiPSC-CMs presenting tachycardia (>300 bpm) and re-entry phenomenon. *B*, parameters measured in the recorded field potential traces: RR interval (n = 8 in each group; Welch's t test, P = 0.0498), QRS interval (n = 8 in each group, P = 0.2786; Mann–Whitney), FPD (n = 8 in each group; Mann–Whitney, P = 0.0019) and FPDcB (n = 8 in each group; Welch's t test, P = 0.0498). *C*, representative field potential traces and parameter changes upon isoprenaline addition in non-isogenic control and

CPVT (UKKi007-A) hiPSC-CMs. *D* and *E*, representative raw data trace showing the dynamic changes of intracellular calcium in response to β-adrenergic stimulation (0.3 and 1 nM isoprenaline), 50 mM KCl and 10 mM caffeine (in 2 mM calcium or 0 calcium solution) in non-isogenic control and CPVT (UKKi007-A) hiPSC-CM. CPVT hiPSC-CMs expressed a high response to the stimulations when compared with the control line and showed spontaneous discharge before or after stimulations. Red arrows indicate the spontaneous discharge. *F*, FRET experimental traces with isoprenaline addition at 2 min and IBMX + FSK at 5 min. FRET ratio at 100 nM isoprenaline peak normalised to saturation level in control (n = 98) and CPVT (n = 70) hiPSC-CMs.

nal calcium spikes remained unaffected by myocytes originating from different cell lines (Fig. 7*C*).

Cardiac action potential measurements of the co-culture using microelectrode arrays demonstrated the functional connection between the neuron and myocyte (Fig. 7*D*). Nicotine stimulation did not alter the myocyte beating rate in cardiac monoculture (Fig. 7*E*); however, it accelerated the beating rate in the neurocardiac co-culture. The increased beating rate was detected 5–23 min after application of nicotine. This observation suggests that neurons in the co-culture were functionally activated by nicotine, conveying neurotransmitters through the synaptic cleft to myocytes and thereby modifying the heart rate. As hyperexcitability was demonstrated in CPVT neurons, we reseeded the CPVT neurons with control myocytes to test whether it triggered arrhythmia. Although no afterdepolarisation was detected in the control myocytes using the microelectrode array, the RR interval of myocytes co-cultured with CPVT neurons was shortened more significantly compared to those co-cultured with control neurons (Fig. 7*F*).

Droplet printing technique for fabricating functional 3D neurocardiac co-cultures using hiPSCs

Human iPSC-derived 3D models provide a more realistic and physiologically relevant platform for studying human biology compared to traditional 2D cell culture systems, where they offer a better recapitulation of the *in vivo* environment in terms of cellular behaviour and function. Recognising the potential of these models, we employed a droplet printing technique to fabricate 3D functional cardiac and SN microtissues derived from hiPSCs. As illustrated in Fig. 8*A*, hiPSC-derived differentiated CMs or SNs were harvested and enzymatically dissociated into single-cell suspensions. To ensure structural integrity and promote cell viability, Matrigel was incorporated into the cell pellet to create a bioink suitable for 3D printing. Using a microfluidic droplet printing approach, we generated 3D microtissues with controlled diameters of approximately 600 μm. These microtissues were then cultured under optimised conditions, fostering the maturation of the printed tissues. By Days 2 or 3, the 3D cardiac microtissues exhibited spontaneous contractions, demonstrating viability and functional activity. These beating cardiac microtissues were then co-cultured with SN microtissues, resulting in the development of 3D neurocardiac co-cultures (Fig. 8*B*). Interestingly, the beating rate in 2D CM monocultures was markedly reduced in 3D cardiac cultures and 3D co-cultures indicating a stabilising action of the microtissue network.

After 7 days of co-culture, we conducted experiments to evaluate the interactions between the cardiac and sympathetic tissues. Immunofluorescence microscopy revealed the distinct presence of CMs, identified by cTnT, and SNs, marked by TH. Notably, neuronal extensions were observed crossing the boundaries between tissues, integrating into the cardiac microtissues (Fig. 8*C* and *D*). This structural and functional integration underscores the utility of 3D co-culture systems for investigating neurocardiac interactions.

Optical mapping reveals enhanced calcium transients in the 3D CPVT model

Irregular calcium activity observed in 3D CPVT microtissues. We demonstrated enhanced intracellular calcium transients in 2D hiPSC-CM CPVT models. To investigate whether this phenomenon can be replicated in 3D models, we utilised optical mapping to monitor calcium dynamics in CPVT and healthy cardiac microtissues. Optical mapping provides high spatial and temporal resolution, enabling non-invasive, real-time monitoring of calcium transients in 3D models. This approach allows for detailed analysis of local and global calcium dynamics, wave propagation and regional variations. As presented in Fig. 8*E*, healthy CM microtissues displayed a smooth activation map and a normal wave pattern (n = 5). In contrast, 12 out of 14 CPVT microtissues displayed irregular, oscillation-like activation maps accompanied by multiple-peaked waves (e.g. CPVT hiPSC-CM2). This observation suggests a continuous calcium leak during calcium release in CPVT cardiac microtissues. Although the beat rate appeared higher in CPVT microtissues compared to healthy controls, the difference was not statistically significant (healthy: 19.53 ± 10.06 bpm, n = 5 microtissues *vs.* CPVT: 52.91 ± 52.48 bpm, n = 11 microtissues; P = 0.1877). However, calcium transient amplitude (CaTA, healthy-CM, 30.69 ± 20.92, n = 5 microtissues; CPVT-CM, 136.4 ± 60.49, n = 11 microtissues; Welch's t test, P = 0.0021) and calcium transient duration at 70% of decay following the peak amplitude (CaTD70, healthy-CM, 350.5 ± 56.08, n = 5 microtissues;

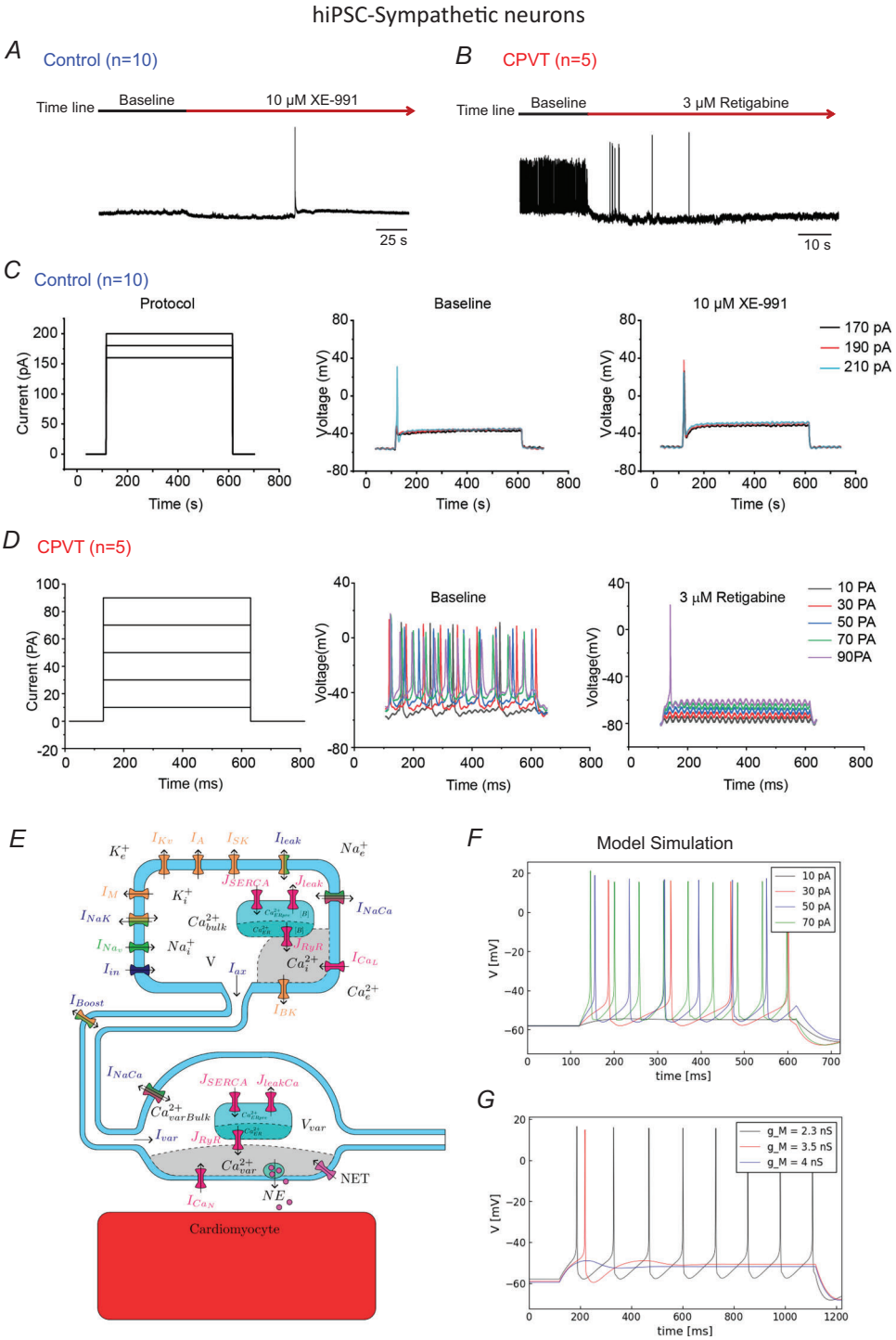

Figure 6. M-current modulation altered neuron firing frequency
A and *B*, example trace of M-current inhibition by 10 μmol/l XE-991 in a control hiPSC-sympathetic neuron and M-current activation by 3 μmol/l retigabine in a CPVT neuron. M-current inhibition increased firing in the control neuron while M-current activation reduced the firing frequency in the CPVT neuron. *C*, in low firing control neurons, M-current inhibition by XE-991 reduced current amplitude required to trigger an action potential from 97±7 to 83±17 pA, $P = 0.03432$ (90%, $n = 10$). *D*, in high firing CPVT neurons, M-current activation by retigabine increased the rheobase amplitude from 12 ± 11 to 73 ± 11 pA, $P = 0.00005$, within 10–90 pA stimulation (100%, $n = 5$). *E*, schematic diagram of computational modelling of sympathetic neurons. I_A, fast K^+ current; I_{ax}, axon inlet current; I_{BK}, big calcium-dependant K^+ current; I_{boost}, axon membrane current; I_{CaL}, L-type Ca^{2+} current; I_{CaN}, N-type Ca^{2+}

current; I_{in}, input stimulus current; I_{leak}, background Na^+ and K^+ currents; I_M, M-type K^+ current; I_{NaCa}, Na^+–Ca^{2+} exchanger; I_{NaK}, Na^+–K^+ pump; I_{NaV}, total Na^+ current; I_{SK}, slow calcium-dependant K^+ current; I_{var}, varicosity inlet current; J_{leak}, endoplasmic reticulum leak flux; J_{RyR}, ryanodine receptor flux; J_{SERCA}, SERCA pump flux; NE, noradrenaline (norepinephrine) concentration; NET, noradrenaline transporter; bulk subscript, bulk intracellular concentration; e subscript, extracellular concentration; i subscript, near-membrane intracellular concentration. *F*, computational model replication of the current clamp results of the CPVT hiPSC-SNs. *G*, plot of computational model voltage showing M-channel upregulation, where g_M is the channel conductance in nanosiemens. This shows the change from tonic to phasic to no-firing. Input current for these simulations is 30 nA.

CPVT-CM, 1447 ± 1018, $n = 11$ microtissues, Welch's t test, $P = 0.0332$) were significantly enhanced in CPVT microtissues (Fig. 8*F*). While differences in beat rate may influence calcium loading and complicate direct comparisons of CaTA and CaTD, the prolonged CaTD in CPVT microtissue suggests that the increased CaTA is not solely due to faster pacing, but may also reflect underlying abnormalities such as sarcoplasmic reticulum calcium leak during reuptake. Consistent with the 2D calcium measurements, we also observed abnormal calcium signalling in the 3D CPVT hiPSC-SN microtissues.

Calcium activity in healthy CMs modulated by CPVT SNs in 3D microtissues. To explore the potential of SN microtissues derived from CPVT to induce arrhythmias in healthy cardiac microtissues, we designed a co-culture experiment. In this set-up, CPVT-derived SN microtissues were co-cultured alongside healthy SN microtissues with healthy cardiac microtissues. This approach allowed us to directly compare the effects of CPVT and healthy SN microtissues on the electrophysiological behaviour and stability of the cardiac microtissues. The dynamic calcium transients were measured exclusively in 3D cardiac microtissues using optical mapping (Fig. 8*G*).

During spontaneous beating, the baseline heart rate, conduction velocity, signal amplitude and CaTD70 remained unchanged in the co-culture containing CPVT-SNs compared to healthy SNs. Following 100 nM nicotine application, the healthy neurocardiac co-culture exhibited an increase in beating rate, but retained normal wave propagation patterns, whereas the co-culture containing CPVT-SNs expressed a reduction of the beat rate with a longer diastolic calcium transient characterised by multi-peaked calcium oscillations (Fig. 8*H*), reflecting sequential spontaneous calcium releases typical of CPVT pathophysiology. Conduction velocity and amplitude were unaffected between the two groups. However, CaTD70 (a measure of calcium transient wave form) was significantly prolonged in co-cultures containing CPVT-SNs (at 1 min: healthy-CM + healthy-SN, 335.1 ± 34.96, $n = 8$; healthy-CM+CPVT-SN, 444.6 ± 131.9, $n = 10$), two-way ANOVA, $P = 0.0393$. Fig. 8*I*). These alterations are likely caused by excessive adrenergic stimulation by NA released by CPVT-SNs, leading to abnormal myocyte calcium release during diastole, increased cytosolic calcium load, and delayed calcium clearance. This dysregulation manifests as delayed activation times, enhanced CaTD70, and the appearance of multi-peaked calcium waves. These abnormalities prevent the calcium wave from returning to baseline, thereby increasing the risk of triggering arrhythmias via enhanced sodium–calcium exchange (Landstrom et al., 2017).

Single-cell RNA sequencing of the diseased transcriptomic phenotype in sympathetic neurons

We sought to understand whether diseased SNs were transcriptomically distinct from healthy counterparts using single-cell RNA sequencing. Following sequencing of CPVT and wild-type hiPSC SN and CM co-cultures and monocultures, QC filtering and dimensionality reduction, we identified approximately three major cell types: neuron, cardiomyocyte and fibroblasts, across around eight major clusters (Fig. 2*C*). SNs clustered into a distinct group as defined by high expression of *GAL* (Kummer, 1987). Differential gene expression analysis between hiPSC SNs from CPVT and wild-type groups highlighted several genes of interest (Fig. 9*A* and *B*). Of particular note is the greater expression in CPVT SNs of one of the major transcription factors driving the SN fate, *PHOX2A* (Stanke et al., 1999), which is essential for expression of catecholaminergic biosynthetic enzymes in a species-dependent manner (Morin et al., 1997). This expression is alongside a number of other markers (*MOXD1*, *MEG3*) implicated across catecholaminergic/sympathetic development, from varying different stages from neural crest cell through to SN, adrenal medullary cells and neuroblastoma (Chan et al., 2019; Fredlund et al., 2023; Gandrillon, 2025), including associations with the cessation of proliferation (*MEG3*; Ye et al., 2020) and terminal differentiation into more mature neuronal phenotypes (*CRABP2*; Harasym et al., 2017). A tempting speculation is that perhaps increased firing rates of CPVT SNs might produce, somewhat paradoxically, a more mature differentiation phenotype. However, this remains for future work to interrogate robustly.

To evaluate pathway-level transcriptional changes between experimental conditions, we performed a non-parametric per-gene differential expression analysis across predefined functional gene groups in our scRNAseq

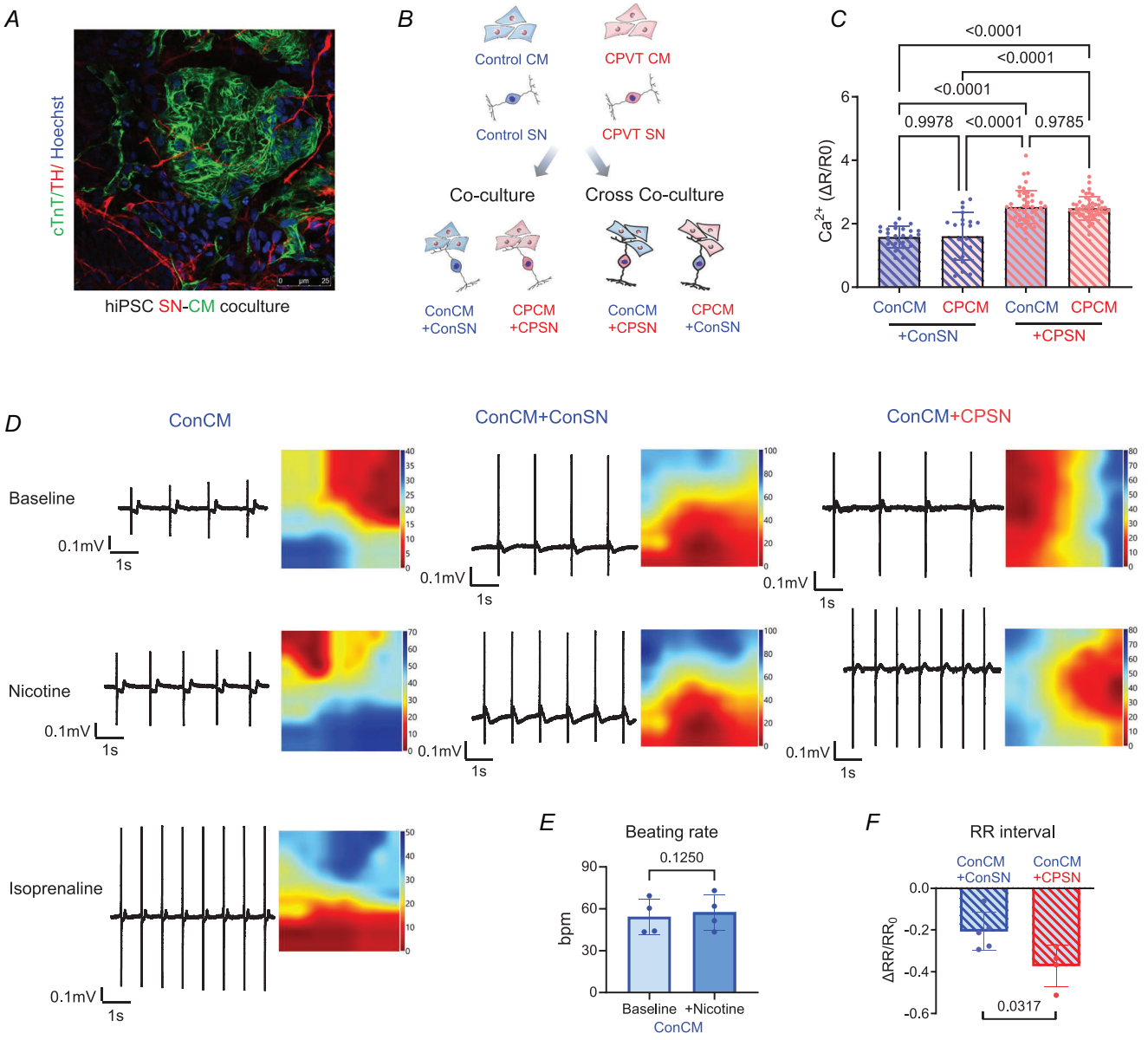

Figure 7. Two-dimensional coculture effect on calcium signalling and electrophysiological properties
A, immunofluorescence showing co-localisation of cardiac and neuronal cell markers in coculture. The overlay of cTnT with TH provided a general impression of the interspersion of neurons and its outgrowth among cardiac myocytes. *B*, schematic diagram of co-culture and cross-culture establishment. *C*, monoculture versus coculture calcium spikes in hiPSC-SN. Cardiac myocytes and sympathetic neurons, derived from either CPVT or control hiPSCs, were co-seeded on coverslips and cultured for 1 week. Upon stimulation with high potassium (50 mM), the calcium release in neurons was significantly higher in CPVT neurons (+ConCM, 2.297 ± 0.62, n = 65 in 6 coveslips; +CPCM, 2.449 ± 0.452, n = 62 in 5 coverslips) compared to their isogenic healthy counterparts (+ConCM, 1.477 ± 0.594, n = 40 in 5 coveslips; +CPCM, 1.071 ± 0.729, n = 50 in 5 coverslips), Kruskal–Wallis test, $P <$ 0.0001. Whether cocultured with healthy myocytes (ConCM) or CPVT myocytes (CPCM), the intracellular calcium concentration in neurons showed no significant alterations. *D*, representative raw data trace showing electrical activity in cardiac myocytes in monoculture and co-culture. The beating rate of monoculture hiPSC-CMs showed a slight increase with 100 μM nicotine, and a significant increase with 1 μM isoprenaline. Nicotine induced a bigger response of myocytes beating rate when they were co-cultured with sympathetic neurons. *E*, group data show that 100 μM nicotine stimulation result in no alteration of the myocyte beating rate in control cardiac monocultures (t test, P = 0.1250). *F*, the reduction of RR interval was more significant in myocytes co-cultured with CPVT neurons (n = 5) compared to control neurons (n = 4, Mann–Whitney test, P = 0.0317).

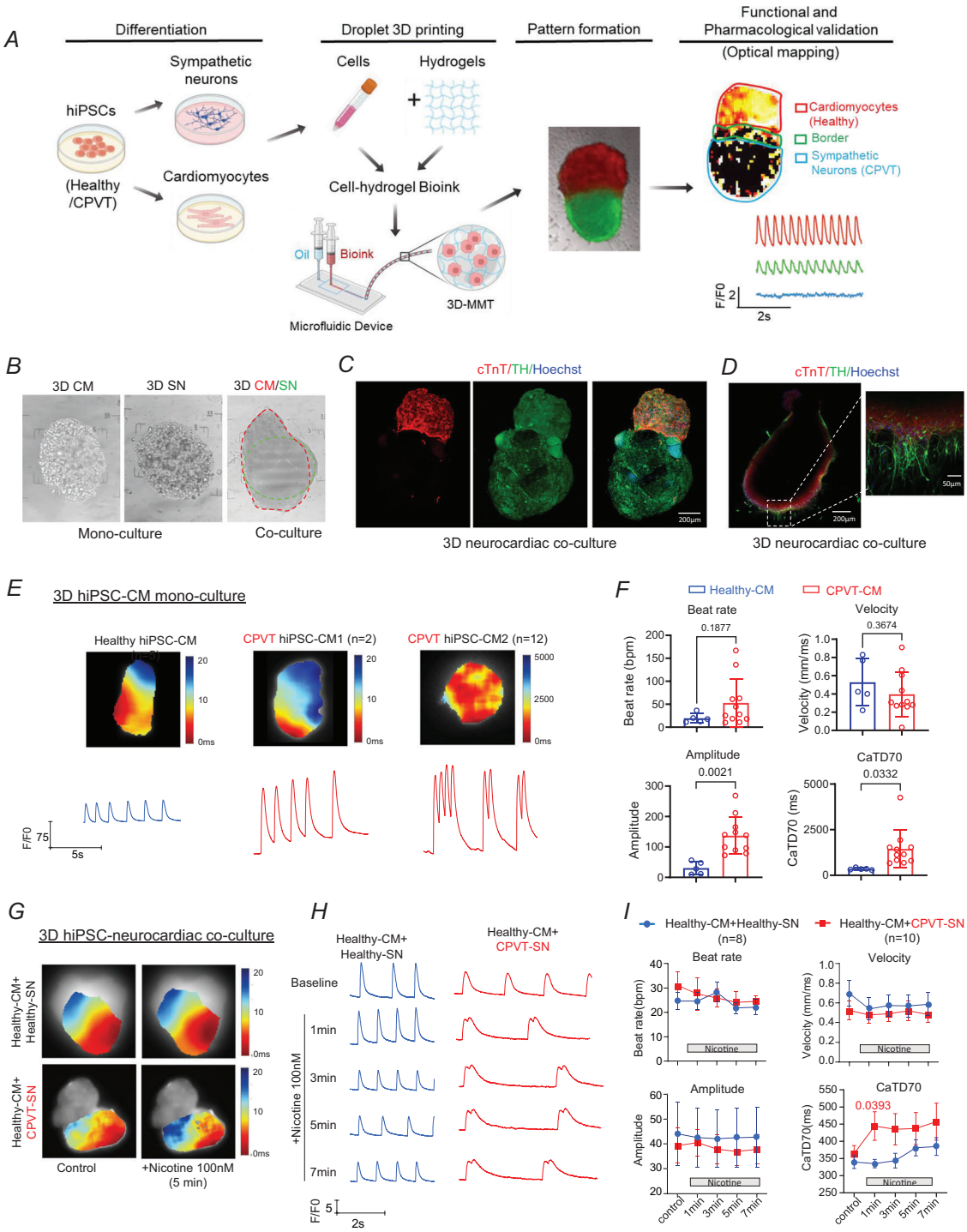

Figure 8. Three-dimensional hiPSC-CM and SN microtissue generation, characterisation and functional phenotypes

A, schematic overview of the 3D cardiac microtissue co-culture experimental workflow. *B*, bright-field microscope images of hiPSC-CM, hiPSC-SN and co-culture of hiPSC-CM/SN, collected with ×10 objective. *C* and *D*, Z-stacked confocal images of hiPSC-CM/SN co-culture: cardiac troponin T (cTnT, red), tyrosine hydroxylase (TH, green) and Hoechst (blue). Neuronal extensions observed to integrate into cardiac microtissues. *E*, optical mapping monitoring of calcium activity in CPVT (n = 11) and healthy (n = 5) hiPSC cardiac microtissues. *F*, amplitude and calcium transient duration at 70% of decay following the peak amplitude (CaTD70) enhanced in CPVT cardiac microtissues. *G*, optical mapping monitoring of calcium activity in healthy hiPSC-CM microtissue co-culture with either healthy control (n = 8) or CPVT (n = 10) hiPSC-SN. *H*, representative optical calcium recordings demonstrated the emergence of multi-peaked calcium transients in cardiac microtissues co-cultured with CPVT-SNs following nicotine

treatment. *I*, grouped data showed significantly prolonged calcium transient duration at 70% decay (CaTD70) in cardiac microtissues co-cultured with CPVT-SNs compared to controls (two-way ANOVA, $P = 0.0393$, compare to baseline).

data. For each analysed cell type (i.e. CM or SN), raw counts were size-normalised and log-transformed according to current best practices (Luecken & Theis, 2019) using the scanpy toolkit for single-cell analyses in Python (Wolf et al., 2018). scRNAseq revealed distinctive transcriptional signatures in CPVT SNs compared to controls (Fig. 10*A*). Within the cAMP synthesis machinery, we observed adenylyl cyclase isoforms, *ADCY1–3*, *ADCY7* and *ADCY8*, showed significant upregulation. Adrenergic receptor expression patterns revealed enhancement of *ADRA2C* only, while β1- and β2-adrenergic receptors (*ADRB1–3*) displayed no significant changes. Examination of phosphodiesterase expression revealed trends towards downregulation of *PDE2A* and *PDE3A*, but these changes were not significant at the single-cell level. However, *PDE3B*

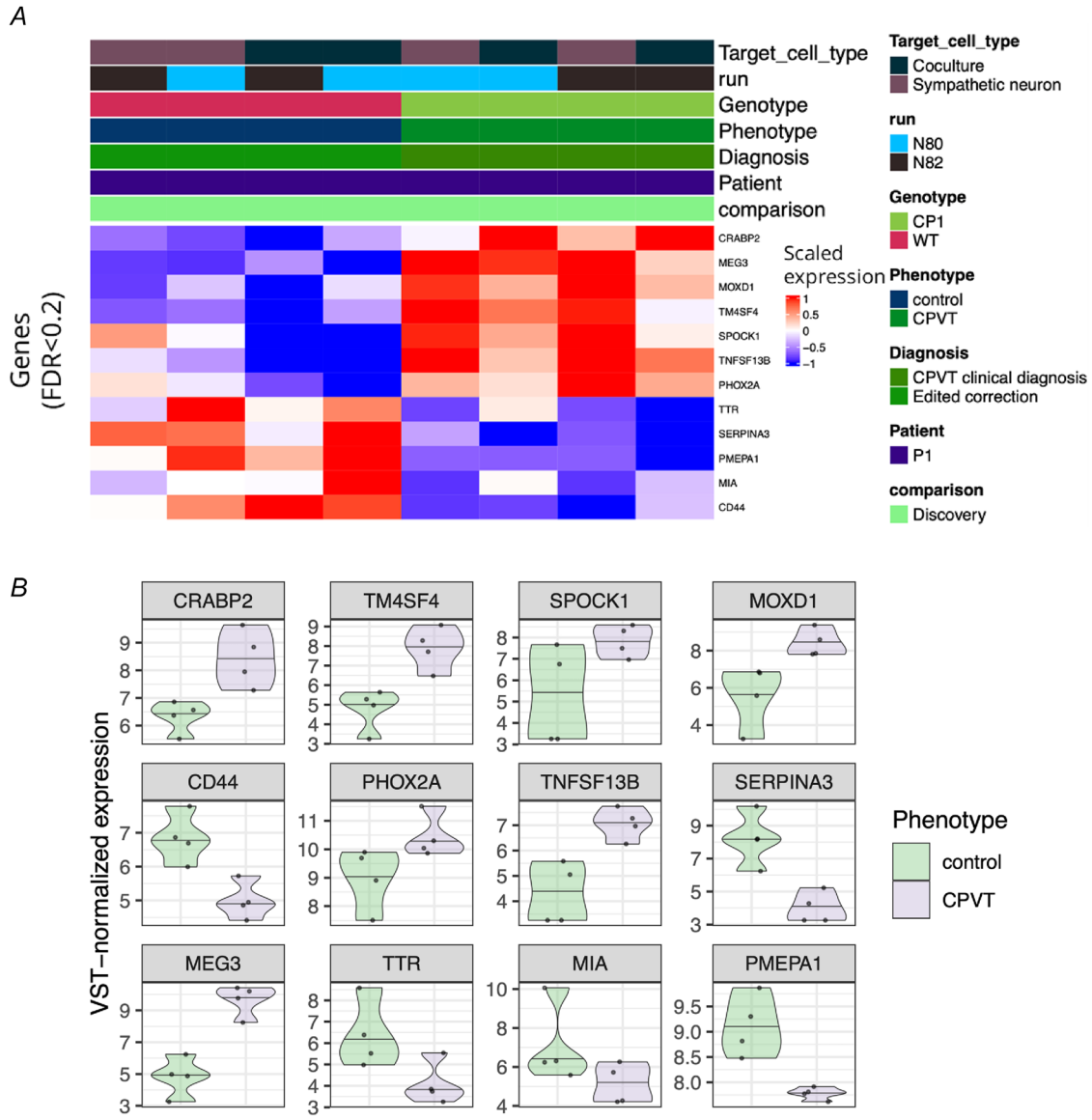

Figure 9. Lists of dysregulated genes in sympathetic neurons due to genotype (FDR < 0.2)
A, 12 differentially expressed genes were identified in eight sympathetic neuron samples. *B*, normalised expression level of these dysregulated genes in control versus CPVT sympathetic neurons. Expression of *CRABP2*, *TM4SF4*, *SPOCK1*, *MOXD1*, *PHOX2A*, *TNFSF13B* and *MEG3* were elevated while *CD44*, *SERPINA3*, *TTR*, *MIA* and *PMEPA1* were reduced in CPVT hiPSC-derived sympathetic neurons.

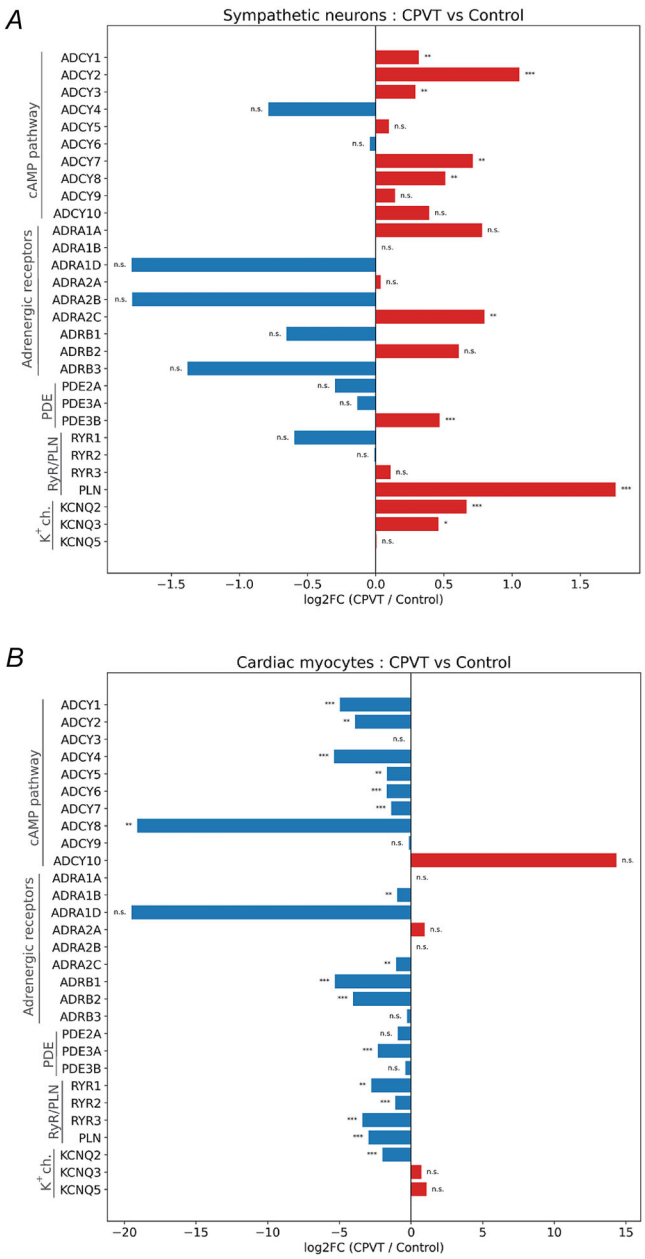

Figure 10. Pathway-level transcriptional changes in hiPSC-derived sympathetic neurons and cardiomyocytes between CPVT and control
Non-parametric per-gene differential expression analysis across predefined functional gene groups in sympathetic neurons (*A*) and cardiomyocytes (*B*): cAMP pathway (adenylyl cyclases *ADCY1-10*), adrenergic receptors (*ADRA1A-2C, ADRB1-3*), phosphodiesterases (*PDE2/3*) and *RyR2/3* and phospholamban (*PLN*). Data shown as log2 fold change (CPVT/control). Blue bars indicate reduced expression; red bars indicate increased expression. Each subplot displays group-specific distributions and associated significance markers (*$P < 0.01$, **$P < 0.0001$, ***$P < 10^{-6}$; n.s., non-significant).

displayed upregulation. Critically, expression of the phospholamban gene, *PLN*, which modulates SERCA by inhibiting its activity, was significantly enhanced in CPVT neurons. These expression profiles suggest enhanced cAMP synthesis capacity (via upregulation of multiple adenylyl cyclase isoforms) coupled with impaired calcium reuptake due to elevated *PLN*, predisposing CPVT SNs to enhanced excitability and excessive neurotransmitter release despite apparent compensatory upregulation of the inhibitory pre-synaptic α2C-autoreceptor (*ADRA2C*) and *PDE3B*. A further source of enhanced $[Ca^{2+}]_i$ may also be related to increased neuronal excitability due to increased expression of *KCNQ2/3*, and downregulation of the channel (loss of function mutation). In CPVT myocytes (Fig. 10*B*), we saw a decrease in β-adrenergic receptors and genes that code for soluble adenylyl cyclase (sAC), a unique, soluble enzyme that produces cAMP in our scRNAseq analysis, suggesting post-synaptic adrenergic signalling to cAMP is depressed to offset the higher levels of cAMP we measured using FRET in CPVT myocytes.

Discussion

CPVT is one of the inherited arrhythmia syndromes associated with a high morbidity rate triggered by activation of the sympathetic nervous system (Pérez-Riera et al., 2018). Although CPVT is regarded as a disease of the cardiomyocyte, we asked the questions whether a component of the disease also resides in the SN, and whether pre-synaptic targeting might present a therapeutic opportunity. This was based on emerging evidence that suggests sympathetic hyperactivity (dysautonomia) may play a critical role in the progression of several primary cardiovascular diseases in driving the adrenergic phenotype in the heart (Larsen et al., 2016; Li & Paterson, 2016; Li, Liu et al., 2022). Recent advances have identified the cardiac RyR2 as a key target for therapeutic intervention, with RyR2 inhibitors showing promise in stabilising intracellular calcium release and reducing arrhythmogenic potential in CPVT models(Do & Knollmann, 2025; Kryshtal et al., 2021).

Here, we provide support for the hypothesis that CPVT may also be a disease of the sympathetic nervous system. We demonstrated a higher frequency of spontaneous calcium discharge and calcium transient amplitude in CPVT hiPSC-CM compared to controls. In the neuron alone, either membrane depolarisation, or an RyR2 receptor agonist, or an acetylcholine receptor agonist triggered whole-cell calcium increases that were significantly higher in CPVT neurons. We observed an increase in unphosphorylated *PLN* in CPVT SNs. This would lead to a greater inhibition of the ER calcium ATPase, which results in shorten calcium re-uptake,

consistent with our greater Ca^{2+} transients in CPVT neurons. Whether flecainide also has its action on neuronal RyR receptors is an attractive hypothesis to test. Nevertheless, calcium is a critical messenger that regulates synaptic plasticity and neurotransmitter release (e.g. Nanou & Catterall, 2018). Thus, dysregulation of calcium signalling in the CPVT SNs could have profound effects on neuronal function and regulation of its target tissues including CMs. This has been seen in pre-hypertensive models of sympathetic dysautonomia where neuronal intracellular calcium transients were significantly larger in stellate neurons and could be reduced by overexpressing activators of cGMP that decreased NA release induced by electric field stimulation (Lu et al., 2015). Given the observed augmentation in calcium transients in the CPVT neurons, an anticipated consequence would be heightened release of NA in the diseased group. Although evoked transmitter release was observed using an ELISA assay and FSCV, reinforcing the notion that the cells were sympathetic in nature, the enhanced calcium responses did not phenocopy onto enhanced transmission in the diseased neurons. This may be related to the developmental state of the neurons still being relatively immature (*ca*. 65 days) and poor statistical power. Nevertheless, several other cellular abnormalities coupled to disrupted calcium homeostasis were identified in the diseased neuron.

PKA phosphorylation is one of the various post-translational modifications of RyR2 receptors that control the release of Ca^{2+} from intracellular stores. Berisha et al. (2021) reported increased β2-AR/cAMP-dependent RyR2 phosphorylation in failing mouse and human myocytes, which increased sarcoplasmic reticulum calcium leak and was arrhythmogenic. Using a cytosolic cAMP FRET sensor, we found an elevation of the concentration of this upstream messenger in hiPSC-CMs in the CPVT groups (UKKi007-A), suggesting an enhanced PKA phosphorylation of RyR2 in the diseased myocytes. Of particular novelty, we also demonstrated an increased cAMP signal in the CPVT hiPSC-SN, which is consistent with the notion that this could facilitate calcium leak in the neuron and potentiate neurotransmission in more mature neurons (Neher & Sakaba, 2008).

In addition to second messenger impairment, dysfunction in ion channels, particularly downregulation of the M-current, has been identified as a contributing factor to abnormal excitability in sympathetic neural firing. Davis et al. (2020) reported a depressed M-current in pre-hypertensive SHR stellate ganglia, which gave rise to a hyperexcitable phenotype. This current is highly conserved and transcripts encoding it have been reported in patients following stellectomy for CPVT (Davis et al., 2020). Here, we also observed the presence of *KCNQ2/3/5* gene in TH-positive hiPSC-SNs (Fig. 2*F*). Of interest, our scRNAseq analysis reports the presence of *KCNQ2/3* in CPVT neurons that co-assemble to form M-current. Although the expression of these transcripts was higher in CPVT neurons (Fig. 10*A*), our results suggest a loss of function mutation may be present, similar to that seen in epilepsy. Consistent with the hypothesis, we also observed hyperexcitability in CPVT neurons with higher spontaneous firing frequency and firing number at rheobase. Activation of the M-current using retigabine was able to stabilise the membrane potential of CPVT neurons, increasing the current injection required to evoke firing. M-current activation may reduce neuronal hyperexcitability in CPVT, but *KCNQ2/3* loss-of-function can cause seizures (Iftimovici et al., 2023). Therapeutic strategies would require careful monitoring and preferably site-specific delivery to cardiac sympathetic ganglia to minimise systemic neurological side effects. Whether upregulation of this current, used in the treatment of neuropathic pain (Rivera-Arconada et al., 2009), has positive clinical utility in CPVT patients to minimise sympathetic-induced arrhythmia remains to be established.

Sympathetic innervation plays a crucial role in influencing cardiac function under normal physiological conditions, but its heightened activity is linked to a diverse spectrum of cardiovascular diseases (Habecker et al., 2025). Oh et al. (2016) were pioneers in reporting functional coupling evidence, demonstrating that NA-secreting SNs in co-culture could drive the heart rate of neonatal CMs when stimulated either pharmacologically or optogenetically. Likewise, other studies have shown that the selective induction of healthy human SNs allows for precise control of CM beating (Takayama et al., 2020; Winbo et al., 2020). This study represents the first exploration of how CPVT-diseased hiPSC-derived SNs interact with CMs in both 2D and 3D neurocardiac co-culture models. CPVT neurons increased myocyte beating rate to a larger extent compared to control neurons at the same level of nicotine stimulation, which was a predictable result as CPVT neurons show hyperexcitability. By measuring the intracellular calcium transient to high K^+ in neurons co-cultured with CMs, the CM was found to have no influence on the neuronal calcium transient amplitude. CPVT neurons still reacted more actively to external stimulation in co-culture. Co-culturing with healthy or CPVT CMs did not alter the calcium elevation in SNs.

Single-cell RNA sequencing was conducted from CPVT and isogenic WT hiPSC-derived CMs and SNs. The isogenic control enabled the preservation of the pathogenic mutation over the pluripotency reprogramming and differentiation process, supporting that impaired calcium handling in both neurons and myocytes is a key component of the disease phenotype. The transcriptome profile identified eight clusters as CMs, SNs, astrocytes,

progenitor neuronal cells, unknown neural cells and fibroblasts. Differential analysis between genotypes filtered out *SERPINA3* as the significantly downregulated gene in CPVT hiPSC SNs. It encodes one member of the serine protease inhibitor family, α-1-antichymotrypsin, which functions to reduce protein degradation. Overall, the balance between α-1-antichymotrypsin and protease activity seems to play an important role in anti-inflammatory, antioxidant, antiangiogenetic, antitumorigenic and antifibrotic processes (Sánchez-Navarro et al., 2021). Whether CPVT is a serpinopathy remains to be determined, but to date, our data suggest this may be the case. How *SERPINA3* downregulation affects sympathetic neuronal activity requires additional experimental investigations to test whether it is related to oxidative stress pathways that are known to upregulate sympathetic transmission (Ko et al., 2019).

Here, we provide a deeper understanding of the arrhythmogenic potential of CPVT-derived neural inputs, shedding light on their pathological interplay. Strategies aimed at directly modulating neurotransmission, either by directly targeting neuronal excitability by increasing M-current or decreasing neuronal cAMP activity by increasing neuronal cGMP (e.g. gene therapy) might provide a therapeutic opportunity alongside modulation of other targets, for example *SERPINA3*. Whether this approach has a gain-of-function over and above the potentially off-targeted action of beta blockers and cardiac stellectomy remains to be determined.

References

Aggarwal, A., Stolear, A., Alam, M. M., Vardhan, S., Dulgher, M., Jang, S.-J., & Zarich, S. W. (2024). Catecholaminergic polymorphic ventricular tachycardia: Clinical characteristics, diagnostic evaluation and therapeutic strategies. *Journal of Clinical Medicine*, **13**(6), 1781.

Argus, F., Zhang, C., Davis, H., Li, N., Tomek, J., Wang, Z. J., Talou, G. M., Li, D., Rodriguez, B., Simoes, F. C., & Paterson, D. J. (2024). A computational model of the sympathetic neuron for drug treatment investigation in sympathetic hyperactivity. *Computing in Cardiology Conference (CinC)*. https://doi.org/10.22489/cinc.2024.142.

Begovic, M., Schneider, L., Zhou, X., Hamdani, N., Akin, I., & El-Battrawy, I. (2024). The role of human-induced pluripotent stem cells in studying cardiac channelopathies. *International Journal of Molecular Sciences*, **25**(22), 12034.

Berisha, F., Götz, K. R., Wegener, J. W., Brandenburg, S., Subramanian, H., Molina, C. E., Rüffer, A., Petersen, J., Bernhardt, A., Girdauskas, E., Jungen, C., Pape, U., Kraft, A. E., Warnke, S., Lindner, D., Westermann, D., Blankenberg, S., Meyer, C., Hasenfuß, G., … Nikolaev, V. O. (2021). cAMP imaging at ryanodine receptors reveals β2-adrenoceptor driven arrhythmias. *Circulation Research*, **129**(1), 81–94.

Cassell, J. F., Clark, A. L., & McLachlan, E. M. (1986). Characteristics of phasic and tonic sympathetic ganglion cells of the guinea-pig. *The Journal of Physiology*, **372**(1), 457–483.

Chan, W. H., Komada, M., Fukushima, T., Southard-Smith, E. M., Anderson, C. R., & Wakefield, M. J. (2019). RNA-seq of isolated chromaffin cells highlights the role of sex-linked and imprinted genes in adrenal medulla development. *Scientific Reports*, **9**(1), 3929.

Coumel, P., Fidelle, J., Lucet, V., Attuel, P., & Bouvrain, Y. (1978). Catecholamine-induced severe ventricular arrhythmias with Adams-Stokes syndrome in children : Report of four cases. *British Heart Journal*, **40**, 28–37.

Davis, H., Herring, N., & Paterson, D. J. (2020). Down-regulation of M current is coupled to membrane excitability in sympathetic neurons before the onset of hypertension. *Hypertension*, **76**(6), 1915–1923.

de Ferrari, G. M., Dusi, V., Spazzolini, C., Bos, J. M., Abrams, D. J., Berul, C. I., Crotti, L., Davis, A. M., Eldar, M., Kharlap, M., Khoury, A., Krahn, A. D., Leenhardt, A., Moir, C. R., Odero, A., Olde Nordkamp, L., Paul, T., Rosés I Noguer, F., Shkolnikova, M., … Schwartz, P. J. (2015). Clinical management of catecholaminergic polymorphic ventricular tachycardia: The role of left cardiac sympathetic denervation. *Circulation*, **131**, 2185–2193.

Do, T. Q., & Knollmann, B. C. (2025). Inhibitors of intracellular RyR2 calcium release channels as therapeutic agents in arrhythmogenic heart diseases. *Annual Review of Pharmacology and Toxicology*, **65**(1), 443–463.

Fatima, A., Xu, G., Shao, K., Papadopoulos, S., Lehmann, M., Arnáiz-Cot, J. J., Rosa, A. O., Nguemo, F., Matzkies, M., Dittmann, S., Stone, S. L., Linke, M., Zechner, U., Beyer, V., Hennies, H. C., Rosenkranz, S., Klauke, B., Parwani, A. S., Haverkamp, W., … Saric, T. (2011). In vitro modeling of ryanodine receptor 2 dysfunction using human induced pluripotent stem cells. *Cellular Physiology and Biochemistry*, **28**(4), 579–592.

Fredlund, E., Andersson, S., Ferreira, M., & Mohlin, S. (2023). Trunk neural crest gene MOXD1 affects embryonic development. bioRxiv. https://doi.org/10.1101/2023.08.29.555314.

Gandrillon, O. (2025). Inferring and simulating a gene regulatory network for the sympathoadrenal differentiation from single-cell transcriptomics in human. bioRxiv. https://www.biorxiv.org/content/10.1101/2025.03.21.644507v3

Gao, J., Makiyama, T., Yamamoto, Y., Kobayashi, T., Aoki, H., Maurissen, T. L., Wuriyanghai, Y., Kashiwa, A., Imamura, T., Aizawa, T., Huang, H., Kohjitani, H., Nishikawa, M., Chonabayashi, K., Fukuyama, M., Manabe, H., Nakau, K., Wada, T., Kato, K., … Kimura, T. (2023). Novel calmodulin variant p.E46K associated with severe catecholaminergic polymorphic ventricular tachycardia produces robust arrhythmogenicity in human induced pluripotent stem cell-derived cardiomyocytes. *Circulation: Arrhythmia and Electrophysiology*, **16**(3), e011387.

Grassi, G., & Drager, L. F. (2024). Sympathetic overactivity, hypertension and cardiovascular disease: State of the art. *Current Medical Research and Opinion*, **40**(sup1), 5–13.

Habecker, B. A., Bers, D. M., Birren, S. J., Chang, R., Herring, N., Kay, M. W., Li, D., Mendelowitz, D., Mongillo, M., Montgomery, J. M., Ripplinger, C. M., Tampakakis, E., Winbo, A., Zaglia, T., Zeltner, N., & Paterson, D. J. (2025). Molecular and cellular neurocardiology in heart disease. *The Journal of Physiology*, **603**(7), 1689–1728.

Harasym, E., McAndrew, N., & Gomez, G. (2017). Sub-micromolar concentrations of retinoic acid induce morphological and functional neuronal phenotypes in SK-N-SH neuroblastoma cells. *In Vitro Cellular, & Developmental Biology Animal*, **53**(9), 798–809.

Hayashi, M., Denjoy, I., Extramiana, F., Maltret, A., Buisson, N. R, Lupoglazoff, J.-M., Klug, D., Hayashi, M., Takatsuki, S., Villain, E., Kamblock, J., Messali, A., Guicheney, P., Lunardi, J., & Leenhardt, A. (2009). Incidence and risk factors of arrhythmic events in catecholaminergic polymorphic ventricular tachycardia. *Circulation*, **119**(18), 2426–2434.

Herring, N., Kalla, M., & Paterson, D. J. (2019). The autonomic nervous system and cardiac arrhythmias: Current concepts and emerging therapies. *Nature Reviews Cardiology*, **16**(12), 707–726.

Iftimovici, A., Charmet, A., Desnous, B., Ory, A., Delorme, R., Coutton, C., Devillard, F., Milh, M., & Maruani, A. (2023). Familial KCNQ2 mutation: A psychiatric perspective. *Psychiatric Genetics*, **34**(1), 24–27.

Itzhaki, I., Maizels, L., Huber, I., Gepstein, A., Arbel, G., Caspi, O., Miller, L., Belhassen, B., Nof, E., Glikson, M., & Gepstein, L. (2012). Modeling of catecholaminergic polymorphic ventricular tachycardia with patient-specific human-induced pluripotent stem cells. *Journal of the American College of Cardiology*, **60**(11), 990–1000.

Joca, H. C, Santos-Miranda, A., Joviano-Santos, J. V., Maia-Joca, R. P. M., Brum, P. C., Williams, G. S. B., & Cruz, J. S. (2020). Chronic sympathetic hyperactivity triggers electrophysiological remodeling and disrupts excitation-contraction coupling in heart. *Scientific Reports*, **10**(1), 8001.

Khemani, P., & Mehdirad, A. A. (2020). Cardiovascular disorders mediated by autonomic nervous system dysfunction. *Cardiology in Review*, **28**(2), 65–72.

Kim, C. W., Aronow, W. S., Dutta, T., Frenkel, D., & Frishman, W. H. (2020). Catecholaminergic polymorphic ventricular tachycardia. *Cardiology in Review*, **28**(6), 325–331.

Ko, E., Kim, J.-S., Bae, J. W, Kim, J., Park, S.-G., & Jung, G. (2019). SERPINA3 is a key modulator of HNRNP-K transcriptional activity against oxidative stress in HCC. *Redox Biology*, **24**, 101217.

Kryshtal, D. O., Blackwell, D. J., Egly, C. L., Smith, A. N., Batiste, S. M., Johnston, J. N., Laver, D. R., & Knollmann, B. C. (2021). RYR2 Channel inhibition is the principal mechanism of flecainide action in CPVT. *Circulation Research*, **128**(3), 321–331.

Kummer, W. (1987). Galanin- and neuropeptide Y-like immunoreactivities coexist in paravertebral sympathetic neurones of the cat. *Neuroscience Letters*, **78**(2), 127–131.

Landstrom, A. P., Dobrev, D., & Wehrens, X. H. T. (2017). Calcium signaling and cardiac arrhythmias. *Circulation Research*, **120**(12), 1969–1993.

Larsen, H. E., Lefkimmiatis, K., & Paterson, D. J. (2016). Sympathetic neurons are a powerful driver of myocyte function in cardiovascular disease. *Scientific Reports*, **6**(1), 38898.

Li, D., Lee, C., Buckler, K., Parekh, A., Herring, N., & Paterson, D. J. (2012). Abnormal intracellular calcium homeostasis in sympathetic neurons from young pre-hypertensive rats. *Hypertension*, **59**(3), 642–649.

Li, D., Liu, K., Davis, H., Robertson, C., Neely, O. C, Tarafdar, A., Li, N., Lefkimmiatis, K., Zaccolo, M., & Paterson, D. J. (2022). Abnormal cyclic nucleotide signaling at the outer mitochondrial membrane in sympathetic neurons during the early stages of hypertension. *Hypertension*, **79**(7), 1374–1384.

Li, D., & Paterson, D. J. (2016). Cyclic nucleotide regulation of cardiac sympatho-vagal responsiveness. *The Journal of Physiology*, **594**(14), 3993–4008.

Li, N., Li, D., Edel, M., Liu, K., Denning, C., & Paterson, D. (2022). Human iPSC derived cardiac myocytes and sympathetic neurons in disease modeling. *Acta Physiologica*, **236**, 609.

Li, N., Li, D., Edel, M., Liu, K., Denning, C., & Paterson, D. (2023). Human iPSC derived cardiac myocytes and sympathetic neurons in disease modelling. *Physiology*, **38**(S1), 5727026.

Li, N., Edel, M., Liu, K., Denning, C., Betts, J., Neely, O. C., Li, D., & Paterson, D. J. (2023). Human induced pluripotent stem cell-derived cardiac myocytes and sympathetic neurons in disease modelling. *Philosophical Transactions of the Royal Society of London. Series B: Biological Sciences*, **378**(1879), 20220173.

Liu, N., Ruan, Y., & Priori, S. G. (2008). Catecholaminergic polymorphic ventricular tachycardia. *Progress in Cardiovascular Diseases*, **51**(1), 23–30.

Lu, C.-J., Hao, G., Nikiforova, N., Larsen, H. E., Liu, K., Crabtree, M. J., Li, D., Herring, N., & Paterson, D. J. (2015). CAPON modulates neuronal calcium handling and cardiac sympathetic neurotransmission during dysautonomia in hypertension. *Hypertension*, **65**(6), 1288–1297.

Luecken, M. D., & Theis, F. J. (2019). Current best practices in single-cell RNA-seq analysis: A tutorial. *Molecular Systems Biology*, **15**(6), e8746.

Ma, S., Mukherjee, N., Mikhailova, E., & Bayley, H. (2017). Gel microrods for 3D tissue printing. *Advanced Biosystem*, **1**(8), e1700075.

Marks, A. R., Priori, S., Memmi, M., Kontula, K., & Laitinen, P. J. (2002). Involvement of the cardiac ryanodine receptor/calcium release channel in catecholaminergic polymorphic ventricular tachycardia. *Journal of Cellular Physiology*, **190**(1), 1–6.

Mazzanti, A., Kukavica, D., Trancuccio, A., Memmi, M., Bloise, R., Gambelli, P., Marino, M., Ortíz-Genga, M., Morini, M., Monteforte, N., Giordano, U., Keegan, R., Tomasi, L., Anastasakis, A., Davis, A. M., Shimizu, W., Blom, N. A., Santiago, D. J., Napolitano, C., … Priori, S. G. (2022). Outcomes of patients with catecholaminergic polymorphic ventricular tachycardia treated with β-blockers. *Journal of the American Medical Association Cardiology*, **7**(5), 504.

Mishra, S., Chander, V., & Kass, D. A. (2025). Cardiac cGMP regulation and therapeutic applications. *Hypertension*, **82**(2), 185–196.

Modell, S. M., & Lehmann, M. H. (2006). The long QT syndrome family of cardiac ion channelopathies: A HuGE review. *Genetics in Medicine*, **8**(3), 143–155.

Morin, X., Cremer, H., Hirsch, M. R., Kapur, R. P., Goridis, C., & Brunet, J. F. (1997). Defects in sensory and autonomic ganglia and absence of locus coeruleus in mice deficient for the homeobox gene Phox2a. *Neuron*, **18**(3), 411–423.

Nanou, E., & Catterall, W. A. (2018). Calcium channels, synaptic plasticity, and neuropsychiatric disease. *Neuron*, **98**(3), 466–481.

Neher, E., & Sakaba, T. (2008). Multiple roles of calcium ions in the regulation of neurotransmitter release. *Neuron*, **59**(6), 861–872.

Oh, Y., Cho, G.-S., Li, Z., Hong, I., Zhu, R., Kim, M.-J., Kim, Y. J, Tampakakis, E., Tung, L., Huganir, R., Dong, X., Kwon, C., & Lee, G. (2016). Functional coupling with cardiac muscle promotes maturation of hPSC-derived sympathetic neurons. *Cell Stem Cell*, **19**(1), 95–106.

Park, S.-J., Zhang, D., Qi, Y., Li, Y., Lee, K. Y., Bezzerides, V. J., Yang, P., Xia, S., Kim, S. L., Liu, X., Lu, F., Pasqualini, F. S., Campbell, P. H., Geva, J., Roberts, A. E., Kleber, A. G., Abrams, D. J., Pu, W. T., & Parker, K. K. (2019). Insights into the pathogenesis of catecholaminergic polymorphic ventricular tachycardia from engineered human heart tissue. *Circulation*, **140**(5), 390–404.

Paton, J. F. R., Żera, T., Vadigepalli, R., Herring, N., & Paterson, D. J. (2025). Multimodal, device-based therapeutic targeting of the cardiovascular autonomic nervous system. *Nature Reviews Cardiology*. Advance online publication. https://doi.org/10.1038/s41569-025-01212-4.

Paudel, R., Jafri, M. S., & Ullah, A. (2024). Gain-of-function and loss-of-function mutations in the RyR2-expressing gene are responsible for the CPVT1-related arrhythmogenic activities in the heart. *Current Issues in Molecular Biology*, **46**(11), 12886–12910.

Pérez-Riera, A. R., Barbosa-Barros, R., de, R. Barbosa, M. P. C., Daminello-Raimundo, R., de Lucca, A. A., & de Abreu, L. C. (2018). Catecholaminergic polymorphic ventricular tachycardia, an update. *Annals of Noninvasive Electrocardiology*, **23**(4), e12512.

Priori, S. G., Napolitano, C., Tiso, N., Memmi, M., Vignati, G., Bloise, R., Sorrentino, V., & Danieli, G. A. (2001). Mutations in the cardiac ryanodine receptor gene (hRyR2) underlie catecholaminergic polymorphic ventricular tachycardia. *Circulation*, **103**(2), 196–200.

Rivera-Arconada, I., Roza, C., & Lopez-Garcia, J. A. (2009). Enhancing m currents: A way out for neuropathic pain? *Frontiers in Molecular Neuroscience*, **2**, 10.

Rojo-Ruiz, J., Rodríguez-Prados, M., Delrio-Lorenzo, A., Alonso, M. T., & García-Sancho, J. (2018). Caffeine chelates calcium in the lumen of the endoplasmic reticulum. *Biochemical Journal*, **475**(22), 3639–3649.

Roston, T. M., Haji-Ghassemi, O., LaPage, M. J., Batra, A. S., Bar-Cohen, Y., Anderson, C., Lau, Y. R., Maginot, K., Gebauer, R. A., Etheridge, S. P., Potts, J. E., Van Petegem, F., & Sanatani, S. (2018). Catecholaminergic polymorphic ventricular tachycardia patients with multiple genetic variants in the PACES CPVT Registry. *PLoS ONE*, **13**(11), e0205925.

Roston, T. M., Jones, K., Hawkins, N. M., Bos, J. M., Schwartz, P. J., Perry, F., Ackerman, M. J., Laksman, Z. W. M., Kaul, P., Lieve, K. V. V., Atallah, J., Krahn, A. D., & Sanatani, S. (2018). Implantable cardioverter-defibrillator use in catecholaminergic polymorphic ventricular tachycardia: A systematic review. *Heart Rhythm*, **15**(12), 1791–1799.

Sánchez-Navarro, A., González-Soria, I., Caldiño-Bohn, R., & Bobadilla, N. A. (2021). An integrative view of serpins in health and disease: The contribution of SerpinA3. *American Journal of Physiology-Cell Physiology*, **320**, C106–C118.

Schneider, L., Begovic, M., Zhou, X., Hamdani, N., Akin, I., & El-Battrawy, I. (2025). Catecholaminergic polymorphic ventricular tachycardia: Advancing from molecular insights to preclinical models. *Journal of the American Heart Association*, **14**, e038308.

Schwartz, P. J., Ackerman, M. J., Antzelevitch, C., Bezzina, C. R., Borggrefe, M., Cuneo, B. F., & Wilde, A. A. M. (2020). Inherited cardiac arrhythmias. *Nature Reviews Disease Primers*, **6**(1), 58.

Stanke, M., Junghans, D., Geissen, M., Goridis, C., Ernsberger, U., & Rohrer, H. (1999). The Phox2 homeodomain proteins are sufficient to promote the development of sympathetic neurons. *Development*, **126**(18), 4087–4094.

Takayama, Y., Kushige, H., Akagi, Y., Suzuki, Y., Kumagai, Y., & Kida, Y. S. (2020). Selective induction of human autonomic neurons enables precise control of cardiomyocyte beating. *Scientific Reports*, **10**(1), 9464.

Tao, T., Paterson, D. J., & Smith, N. P. (2011). A model of cellular cardiac-neural coupling that captures the sympathetic control of sinoatrial node excitability in normotensive and hypertensive rats. *Biophysical Journal*, **101**(3), 594–602.

Webster, G., & Berul, C. I. (2013). An update on channelopathies: From mechanisms to management. *Circulation*, **127**(1), 126–140.

Wehrens, X. H. T., Lehnart, S. E., Reiken, S. R., Deng, S.-X., Vest, J. A., Cervantes, D., Coromilas, J., Landry, D. W., & Marks, A. R. (2004). Protection from cardiac arrhythmia through ryanodine receptor-stabilizing protein calstabin2. *Science*, **304**(5668), 292–296.

Winbo, A., Ramanan, S., Eugster, E., Jovinge, S., Skinner, J. R., & Montgomery, J. M. (2020). Functional coculture of sympathetic neurons and cardiomyocytes derived from human-induced pluripotent stem cells. *American Journal of Physiology-Heart and Circulatory Physiology*, **319**(5), H927–H937.

Wleklinski, M. J., Kannankeril, P. J., & Knollmann, B. C. (2020). Molecular and tissue mechanisms of catecholaminergic polymorphic ventricular tachycardia. *The Journal of Physiology*, **598**(14), 2817–2834.

Wolf, F. A., Angerer, P., & Theis, F. J. (2018). SCANPY: Large-scale single-cell gene expression data analysis. *Genome Biology*, **19**(1), 15

Wolf, K., Zarkua, G., Chan, S.-A., Sridhar, A., & Smith, C. (2016). Spatial and activity-dependent catecholamine release in rat adrenal medulla under native neuronal stimulation. *Physiological Reports*, **4**(17), e12898.

Yang, X., Artibani, M., Jin, Y., Aggarwal, A., Zhang, Y., Muñoz-Galvan, S., Mikhailova, E., Rai, L., Mukherjee, N., Kumar, R. K., Albukhari, A., Zhou, L., Ahmed, A. A., & Bayley, H. (2023). A 3D microtumour system that faithfully represents ovarian cancer minimal residual disease. *Advanced Healthcare Materials*, **14**(14), e2404072.

Ye, M., Lu, H., Tang, W., Jing, T., Chen, S., Wei, M., Zhang, J., Wang, J., Ma, J., Ma, D., & Dong, K. (2020). Down-regulation of MEG3 promotes neuroblastoma development through FOXO1-mediated autophagy and mTOR-mediated epithelial-mesenchymal transition. *International Journal of Biological Sciences*, **16**(15), 3050–3061.

Additional information

Data availability statement

Data are available from the corresponding author upon reasonable request.

Competing interests

The authors declare no conflict of interest.

Author contributions

Experimental design and supervision: D.L. and D.J.P.; methodology: N.L., E.M.T., L.Z., C.S., G.H., D.L. and D.J.P.; investigation: N.L., C.Z., M.X., Y.Y.C., R.D., X.H., C.A.P, F.A., K.L., D.S.O., M.L., C.S. and D.L.; resources: H.B., C.D., A.I.D. and G.H.; funding acquisition: D.J.P. and A.I.D.; writing (original draft): N.L. and D.L.; writing (review and editing): D.L. and D.J.P. All authors have read and approved the final version of this manuscript and agree to be accountable for all aspects of the work in ensuring that questions related to the accuracy or integrity of any part of the work are appropriately investigated and resolved. All persons designated as authors qualify for authorship, and all those who qualify for authorship are listed.

Funding

This work was supported by the British Heart Foundation (SP/F/22/150027), the Leducq International Network of Excellence Award (24CVD), ERC consolidator award (ERC-2017 COG 771431) and BBSRC (BB/Y006488/1).

Acknowledgements

We thank Alexander Grassam-Rowe for critical reading and valuable comments on this manuscript and Shunan Zhang for technical assistance. We thank Dr Michael Edel for initial advice on stem cell development.

Keywords

catecholaminergic polymorphic ventricular tachycardia, hiPSC, microtissue, neurocardiac co-culture

Supporting information

Additional supporting information can be found online in the Supporting Information section at the end of the HTML view of the article. Supporting information files available:

Peer Review History

Translational perspective

Catecholaminergic polymorphic ventricular tachycardia (CPVT) is a genetic disorder causing life-threatening heart rhythm disturbances in young people, triggered by stress or exercise. Despite treatment with beta-blocking medications, 10–30% of patients continue experiencing potentially fatal arrhythmias. Although surgically removing sympathetic nerves that regulate the heart (stellate ganglionectomy) can be effective (albeit with side effects), treatments have traditionally focused on correcting defects in heart muscle cells rather than targeting the nervous system. This study hypothesised that the genetic mutations causing CPVT also reside in the sympathetic nerve cells and enhance cardiac excitability. Using human induced pluripotent stem cells from CPVT patients and healthy controls, we generated both heart muscle cells and sympathetic neurons, examining their function individually and in co-culture (2D and 3D). Our findings reveal that CPVT neurons are hyperexcitable with abnormal calcium handling and elevated cyclic AMP signalling. Most importantly, when diseased neurons were paired with healthy heart cells, they triggered abnormal rhythms, establishing that neuronal dysfunction directly causes cardiac arrhythmias. These results provide a mechanistic explanation for why nerve surgery benefits CPVT patients and reframes the disease as a neuro-cardiac disorder rather than purely a heart condition. This paradigm shift opens therapeutic avenues targeting the nervous system through precise neuromodulation, such as drugs enhancing M-type potassium channels to reduce neuronal excitability, or interventions normalising neuronal cAMP levels. Such approaches could offer more specific treatment options while avoiding the risks and irreversibility of surgical sympathetic denervation.